

Banner appropriate to article type will appear here in typeset article

# Vortex dynamics of accelerated flow past a mounted wedge

Jiten C. Kalita<sup>1</sup> and Pankaj Kumar<sup>2</sup>†

<sup>1</sup>Department of Mathematics, Indian Institute of Technology Guwahati, Guwahati 781039, Assam, India

<sup>2</sup>Department of Mechanical Engineering, Indian Institute of Technology Guwahati, Guwahati 781039, Assam, India

(Received xx; revised xx; accepted xx)

This study is concerned with the simulation of a complex fluid flow problem involving flow past a wedge mounted on a wall for channel Reynolds numbers  $Re_c = 1560, 6621$  and  $6873$  in uniform and accelerated flow medium. The transient Navier-Stokes (N-S) equations governing the flow has been discretized using a recently developed second order spatially and temporally accurate compact finite difference method on a nonuniform Cartesian grid by the authors. All the flow characteristics of a well-known laboratory experiment of Pullin and Perry (1980) have been remarkably well captured by our numerical simulation, and we provide a qualitative and quantitative assessment of the same. Furthermore, the influence of the parameter  $m$ , controlling the intensity of acceleration, has been discussed in detail along with the intriguing consequence of non-dimensionalization of the N-S equations pertaining to such flows. The simulation of the flow across a time span significantly greater than the aforesaid lab experiment is the current study's most noteworthy accomplishment. For the accelerated flow, the onset of shear layer instability leading to a more complicated flow towards transition to turbulence have also been aptly resolved. The existence of coherent structures in the flow validates the quality of our simulation, as does the remarkable similarity of our simulation to the high Reynolds number experimental results of Lian and Huang (1989) for the accelerated flow across a typical flat plate. All three steps of vortex shedding, including the exceedingly intricate three-fold structure, have been captured quite efficiently.

**Keywords:**

**Mathematics Subject Classifications:**

## 1. Introduction

Owing to the intrinsic and complicated characteristics of the flow phenomena, especially the separation of flows, research on flow past sharp edges of bluff bodies has attracted a great deal of interest for many years. Here, the boundary layer gets constricted near the edge, intensifies and eventually forms a vortex. The boundary layer separates and forms a coherent spiral shear-layer as the vortex evolves in intensity and size, which is actually a roll-up characteristic of vortex formation. These flows can be used to investigate the free

† Email address for correspondence: jiten@iitg.ac.in

shear layer and vortex dynamics. The current study aims to investigate a classic example of fluid flow past a bluff body with a sharp edge, namely flow past a wedge.

The flow past a thin plate normal to the free stream is a classic example of bluff body flow, which corresponds to wedges with zero angle of incidence. Prandtl (1904) was the pioneer in such studies, who experimented with the flow past a normal flat plate in 1904 in the first study of this kind. Later, Anton (1956) and Wedemeyer (1961) presented their experimental studies for the same. Pierce (1961) used the spark shadowgraph technique to show photographic evidence of separation at sharp angles. Taneda and Honji (1971) employed the aluminum dust method to visualize the flow past impulsively started and uniformly accelerated flat plates. Lian and Huang (1989) used the hydrogen bubble technique to visualize the flow past accelerating plates. Dennis et al. (1993) did an experimental investigation for the impulsively started flat plate at moderate Reynolds numbers. In a similar fashion, Pullin and Perry (1980) used dye in water to study the development of the separating shear layer past thin and thick wedges. They presented the trajectory of the vortex center through detailed analysis for different acceleration parameters  $m$  and wedge angles. They also compared their observations via inviscid similarity theory Kaden (1931); Pullin (1978). Recent experiments are seen to focus their attention on studying the leading-edge flow past a plate and three-dimensional tip vortex effects Kriegseis et al. (2013); Ringuette et al. (2007)) associated with it. Another study worth mentioning in this direction is that of Koumoutsakos and Shiels (1996), who numerically simulated the flow past an impulsively started ( $m = 0$ ) and uniformly accelerated ( $m = 1$ ) flat plates.

In contrast to other bluff body flows, the wedge's separation point is marked by a sharp edge. Although it appears to be easy, obtaining the numerical solutions are difficult owing to edge singularity. Many scholars have published analytical results for this sort of flow Villat (1930); Wedemeyer (1961); Pullin (1978); Krasny (1991)) assuming inviscid evolution of the vorticity field by properly assessing circulation growth at the wedge tip and distant from it. Furthermore, numerical simulation of these types of flows is difficult due to the singularities at the tips. As a result, the majority of the computational techniques devised to explore this flow were initially limited to steady-state flow for low and moderate Reynolds values. To avoid singularity, one way is to construct an extremely fine grid around the edge.

Davies et al. (1995) (in 1995) numerically studied the interactions of coastal currents with topographic indentations that mimics the flow past a sharp wedge. Recently, Xu and Nitsche (2015) numerically studied viscous flow past a flat plate in accelerating flow. Their results were in good agreement with the experimental study of Pullin and Perry (1980) for thin wedges with an angle of  $5^\circ$ . Xu (2016) then numerically studied vortex formation in the impulsively started viscous flow past an infinite wedge for wedge angles ranging from  $60^\circ$  to  $150^\circ$  in uniform flow, where potential flow theory was employed to solve this problem. All the previous research, both experimental and numerical Kiya and Matsumura (1988); Perry and Steiner (1987); Kiya and Arie (1980); Chein and Chung (1988); Tamaddon-Jahromi et al. (1994), including those by Pullin and Perry (1980) and Xu and Nitsche (2015); Xu (2016) on the flat plate or wedge, were conducted only for the early part in the near wake region.

The current research is mainly inspired by the experimental visualization of Pullin and Perry (1980) for the flow past a mounted wedge for an wedge angle  $60^\circ$ . Our study attempts to build on other previous works of research ( Pullin (1978); Koumoutsakos and Shiels (1996); Xu and Nitsche (2015); Xu (2016)) by addressing flow simulation in the following two areas: uniform flow in laminar region for channel Reynolds number  $Re_c = 1560$  and accelerated flow till transition to turbulence from laminar state for  $Re_c = 6621$   $Re_c = 6873$ . A recently developed second order spatially and temporally accurate compact finite difference method on a nonuniform Cartesian grid by the authors (Kumar and Kalita (2020)) has been used to

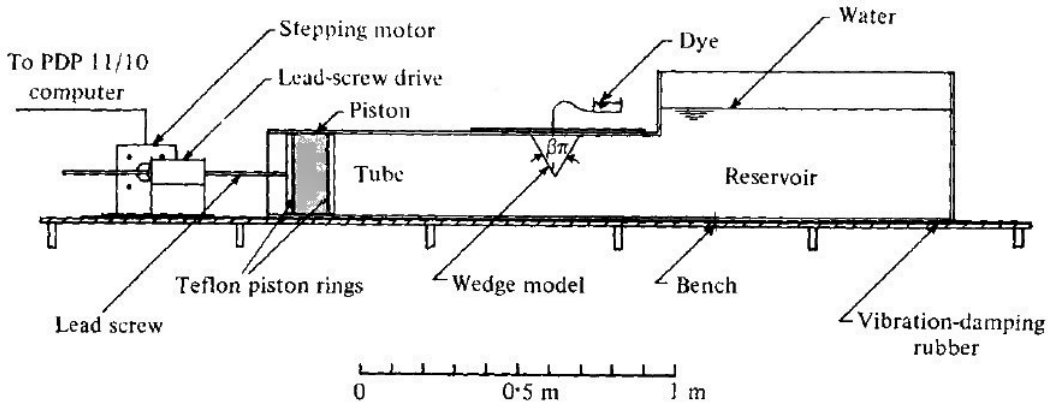


Figure 1: Experimental set-up for starting vortex flow visualization by (Pullin and Perry (1980)). The movement of the piston, shown in shade, generates the acceleration in the flow.

discretize the transient Navier-Stokes equations governing the flow. Apart from replicating the flow visualization of Pullin and Perry (1980) for the earliest part of the flow, where the flow was stopped at a non-dimensional time much less than unity, we continued our simulations up to a non-dimensional time  $t = 3.0$ . This allowed us to observe hitherto unreported vortex structures, which were observed earlier only in the experimental visualization of accelerated flow past a flat plate (Lian and Huang (1989)). We have also provided a detailed account of the flow separation, vortex formation and the movement of the vortex centers for  $Re_c = 6873$ , which has not been reported earlier.

The paper has been arranged in six sections. Section 2 deals with the flow description and the governing equations, section 3 with a brief discussion on discretization procedure and numerical method, section 4, and finally, section 5 summarizes the whole work.

## 2. The flow description and the governing equations

The problem considered here is the accelerated flow past a wedge mounted on a wall, which was experimentally carried out by Pullin and Perry (1980). The experimental set-up used by them for the starting vortex flow visualization is reproduced in figure 1. The wedge of height  $h$  is kept normal to the accelerated flow in a channel of width  $H$  and is fixed to the wall with an angle  $60^\circ$ , defined as the wedge angle  $\theta = \beta\pi$ , so that the case undertaken here corresponds to  $\beta = \frac{1}{3}$ . The flow was driven by the rectangular piston as shown in the figure, which was also responsible for imparting acceleration to the flow. Note that flow past a flat plate is a limiting example of flow past a wedge of zero angle. This sharp edge fixes the point of separation which leads to generation of spiral shear layer and vortex formation. For other details of the set-up, readers may refer to the same work by Pullin and Perry (1980).

The flow is governed by the Navier-Stokes equations for incompressible viscous flows, the streamfunction-velocity ( $\psi-v$ ) formulation (Gupta and Kalita (2005); Kalita and Gupta (2010); Sen et al. (2013); Sen and Kalita (2015)) of which, in dimensional form, can be written as

$$\frac{\partial}{\partial \tilde{t}}(\nabla^2 \tilde{\psi}) = \nu \nabla^4 \tilde{\psi} + \tilde{u} \nabla^2 \tilde{v} - \tilde{v} \nabla^2 \tilde{u}, \quad (2.1)$$

where the quantities  $\tilde{t}$ ,  $\tilde{\psi}$ ,  $\tilde{u}$ ,  $\tilde{v}$  are respectively time, streamfunction, and velocities along the

Table 1: Flow parameters used in the current study.

m	A ( $cm s^{-(1+m)}$ )	$Re_c$	$\tilde{t}_f$ (s)	$t_f$
0	0.63	1560	12.52	0.310535
0.45	0.86	6621	5.96	0.577061
0.88	0.38	6873	7.08	0.757289

horizontal  $\tilde{x}$ - and vertical  $\tilde{y}$ -directions and  $\nu$  is the kinematic viscosity. Their units are  $\tilde{t}$  (s),  $\tilde{\psi}$  ( $cm^2 s^{-1}$ ),  $\tilde{u}$  ( $cms^{-1}$ ),  $\tilde{v}$  ( $cms^{-1}$ ) and  $\nu$  ( $cm^2 s^{-1}$ ).

The  $\psi$ - $\nu$  formulation can easily be written in pure Streamfunction form as

$$\frac{\partial}{\partial \tilde{t}}(\nabla^2 \tilde{\psi}) = \nu \nabla^4 \tilde{\psi} - \frac{\partial \tilde{\psi}}{\partial \tilde{y}} \frac{\partial}{\partial \tilde{x}} \nabla^2 \tilde{\psi} + \frac{\partial \tilde{\psi}}{\partial \tilde{x}} \frac{\partial}{\partial \tilde{y}} \nabla^2 \tilde{\psi} \quad (2.2)$$

As mentioned earlier, the flow is driven by the piston moving with a velocity  $\tilde{v}_p = \tilde{u}_0 + A\tilde{t}^m$  where  $\tilde{u}_0$  (set as zero in the actual experiment) is the velocity at the inlet,  $A$  and  $m$  are pre-chosen constants.  $\tilde{v}_p$  enables acceleration of the viscous fluid. For example,  $m = 0$  renders a uniform velocity at the inlet indicating an impulsive start, while  $m = 1$  and  $2$  stand for uniform and linear acceleration respectively Xu and Nitsche (2015). Equations (2.1)-(2.2) are non-dimensionalized using the channel width  $H$  and, the constants  $A$  and  $m$ . Defining the non-dimensional variables

$$(x, y) = \frac{(\tilde{x}, \tilde{y})}{H}, (u, v) = \frac{(\tilde{u}, \tilde{v})}{H \left(\frac{A}{H}\right)^{\frac{1}{1+m}}}, \psi = \frac{\tilde{\psi}}{H^2 \left(\frac{A}{H}\right)^{\frac{1}{1+m}}} \text{ and } t = \frac{\tilde{t}}{\left(\frac{H}{A}\right)^{\frac{1}{1+m}}}, \quad (2.3)$$

equation (2.1) in non-dimensional form can be written as

$$\frac{\partial}{\partial t}(\nabla^2 \psi) = \frac{1}{Re_c} \nabla^4 \psi + u \nabla^2 v - \nu \nabla^2 u, \quad (2.4)$$

where  $Re_c$  is the channel Reynolds number defined as  $Re_c = \frac{H^2 \left(\frac{A}{H}\right)^{\frac{1}{1+m}}}{\nu}$  (Pullin and Perry (1980)). For the values of  $m$  used in this study, the dimensional variables can be retrieved by using the following table 1 where apart from tabulating the pre-chosen constants  $A$ ,  $m$  and the corresponding channel Reynolds numbers  $Re_c$ , we have also provided the instants of time at which the experiments were stopped and the corresponding non-dimensional times following (2.3).

Pullin and Perry (1980) also introduced a scale Reynolds number defined by

$$Re_s(\tilde{t}) = \alpha_0^{\frac{2}{2-n}} \left[ \left(\frac{A}{H}\right)^{\frac{1}{1+m}} \tilde{t} \right]^{2M-1} Re_c, \quad (2.5)$$

with  $n = \frac{1}{2-\beta}$ ,  $M = \frac{1+m}{2-n}$  and  $\alpha_0$  is a dimensionless constant whose value depends on the wedge angle  $\beta\pi$  and can be found from figure 14 of Pullin and Perry (1980). Note that the expression within the parenthesis on the right hand side of (2.5) is the non-dimensional time



and therefore (2.5) may be recast as

$$Re_s(t) = \alpha_0^{\frac{2}{2-n}} t^{2M-1} Re_c, \quad (2.6)$$

which will be used to show the trajectory of the scaled vortex center later on in section 4.4.

### 3. Discretization and numerical method

A second order time and space accurate compact finite difference scheme has recently been devised (Kumar and Kalita (2020)) for the  $\psi$ - $v$  form of the transient-state Navier-Stokes (N-S) equations on nonuniform Cartesian grids without transformation. On a nine point stencil, equation (2.4) in discretized form has the following form:

$$\begin{aligned} & \frac{2}{x_f + x_b} \left[ \frac{\psi_{i+1,j}^{n+1}}{x_f} + \frac{\psi_{i-1,j}^{n+1}}{x_b} - \left( \frac{1}{x_f} + \frac{1}{x_b} \right) \psi_{i,j}^{n+1} \right] + \frac{2}{y_f + y_b} \left[ \frac{\psi_{i,j+1}^{n+1}}{y_f} + \frac{\psi_{i,j-1}^{n+1}}{y_b} - \left( \frac{1}{y_f} + \frac{1}{y_b} \right) \psi_{i,j}^{n+1} \right] \\ &= \frac{0.5\Delta t}{Re_c} \left\{ \left( A\psi_{i+1,j+1}^n + B\psi_{i,j+1}^n + C\psi_{i-1,j+1}^n + D\psi_{i+1,j}^n + E\psi_{i,j}^n + F\psi_{i-1,j}^n + G\psi_{i+1,j-1}^n + H\psi_{i,j-1}^n \right. \right. \\ & \left. \left. + I\psi_{i-1,j-1}^n \right) - \phi_{i,j}^n \right\} + \frac{0.5\Delta t}{Re_c} \left\{ \left( A\psi_{i+1,j+1}^{n+1} + B\psi_{i,j+1}^{n+1} + C\psi_{i-1,j+1}^{n+1} + D\psi_{i+1,j}^{n+1} + E\psi_{i,j}^{n+1} + F\psi_{i-1,j}^{n+1} \right. \right. \\ & \left. \left. + G\psi_{i+1,j-1}^{n+1} + H\psi_{i,j-1}^{n+1} + I\psi_{i-1,j-1}^{n+1} \right) - \phi_{i,j}^{n+1} \right\} \\ & + \frac{2}{x_f + x_b} \left[ \frac{\psi_{i+1,j}^n}{x_f} + \frac{\psi_{i-1,j}^n}{x_b} - \left( \frac{1}{x_f} + \frac{1}{x_b} \right) \psi_{i,j}^n \right] + \frac{2}{y_f + y_b} \left[ \frac{\psi_{i,j+1}^n}{y_f} + \frac{\psi_{i,j-1}^n}{y_b} - \left( \frac{1}{y_f} + \frac{1}{y_b} \right) \psi_{i,j}^n \right] \\ & + \frac{x_f - x_b}{x_f + x_b} \left[ \frac{v_{i+1,j}^n}{x_f} + \frac{v_{i-1,j}^n}{x_b} - \left( \frac{1}{x_f} + \frac{1}{x_b} \right) v_{i,j}^n \right] - \frac{y_f - y_b}{y_f + y_b} \left[ \frac{u_{i,j+1}^n}{y_f} + \frac{u_{i,j-1}^n}{y_b} - \left( \frac{1}{y_f} + \frac{1}{y_b} \right) u_{i,j}^n \right] \\ & + \frac{x_f - x_b}{x_f + x_b} \left[ \frac{v_{i+1,j}^{n+1}}{x_f} + \frac{v_{i-1,j}^{n+1}}{x_b} - \left( \frac{1}{x_f} + \frac{1}{x_b} \right) v_{i,j}^{n+1} \right] - \frac{y_f - y_b}{y_f + y_b} \left[ \frac{u_{i,j+1}^{n+1}}{y_f} + \frac{u_{i,j-1}^{n+1}}{y_b} - \left( \frac{1}{y_f} + \frac{1}{y_b} \right) u_{i,j}^{n+1} \right] \end{aligned} \quad (3.1)$$

Where  $\Delta t$  is the uniform time step and  $x_f$ ,  $x_b$ ,  $y_f$ ,  $y_b$  are the nonuniform forward and backward step-lengths in the  $x$  and  $y$  directions, respectively. The horizontal and vertical velocities, respectively  $u$  and  $v$ , can be retained using  $u = \frac{\partial \psi}{\partial y}$  and  $v = -\frac{\partial \psi}{\partial x}$ . Using this relations, the following implicit relation can be used to approximate the horizontal velocity up to third order accuracy.

$$\begin{aligned} \frac{y_b}{2k} u_{i,j+1} - 2u_{i,j} + \frac{y_f}{2k} u_{i,j-1} &= \frac{3(\psi_{i,j+1} - \psi_{i,j-1})}{2k} - \frac{3(y_f - y_b)}{2k} \left[ \frac{\psi_{i,j+1}}{y_f} + \frac{\psi_{i,j-1}}{y_b} - \left( \frac{1}{y_f} + \frac{1}{y_b} \right) \psi_{i,j} \right] \\ &+ O(y_f y_b (y_f - y_b)). \end{aligned} \quad (3.2)$$

The renowned tridiagonal solver Thomas algorithm Anderson Jr (1995); Pletcher et al. (2012) is used to solve the algebraic system produced by (3.2). Similar calculations can be used to approximate the vertical velocity,  $v$ . In addition to the derivation of the equations (3.1) through (3.2), the specifics of the coefficients  $A$ ,  $B$ ,  $C$ ,  $D$ ,  $E$ ,  $F$ ,  $G$ ,  $H$ ,  $I$  and the

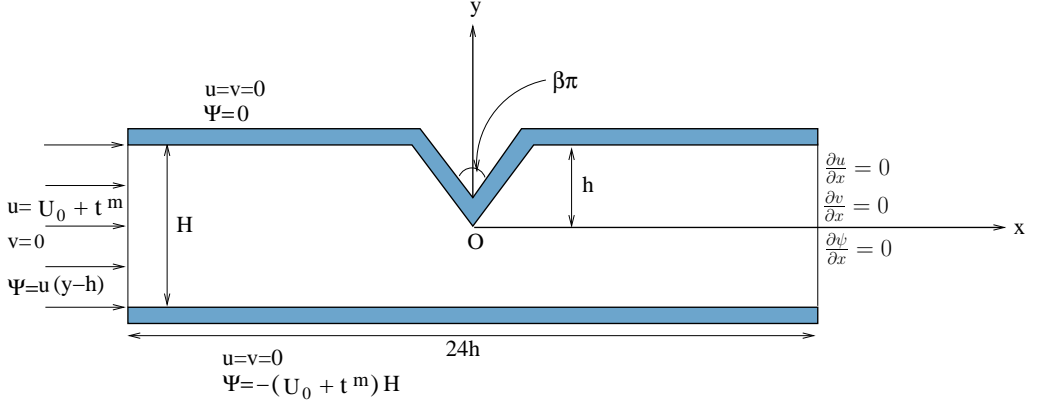


Figure 2: Problem statement of flow past a wedge in accelerated flow.

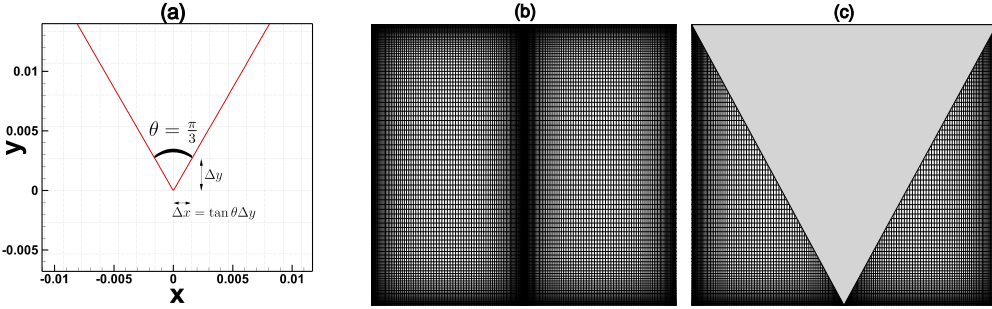


Figure 3: The grid generating strategy: (a) the transformation used, (b) the fundamental block and (c) the wedge implanted on the block.

function  $\phi$  can be found in Kumar and Kalita (2020). The vorticity  $\omega$ , when required can be post-processed from the relation  $\omega = \frac{\partial v}{\partial x} - \frac{\partial u}{\partial y}$ .

The schematic of the flow along with boundary conditions used in our computation is shown in figure 2. The fluid is assumed to be flowing from left to right. Note that use of equation (2.3) for non-dimensionalization renders the piston velocity  $\tilde{v}_p = \tilde{u}_0 + A\tilde{t}^m$  to  $u = U_0 + t^m$  at non-dimensional time  $t$  where  $U_0$  is the inlet velocity at  $t = 0$ . The dimensions of the computational domain was set as  $-6.0 \leq x \leq 6.0$  and  $-0.5 \leq y \leq 0.5$  such that the width of the channel is unity and the tip of the wedge is located at the origin. Following Pullin and Perry (1980), the ratio of the channel width and wedge-height is kept at 2 : 1 as well. The boundary conditions at the inlet is taken as  $u = U_0 + t^m$ ,  $v = 0$  and  $\psi = u(y - h)$ .  $\psi$  is scaled this way in order to attain a value zero on the top wall, i.e.,  $\psi_{top} = 0$  and the same streamline corresponding to  $\psi = 0$  continues its journey by touching the wedge surface. Consequently boundary conditions for  $\psi$  at the bottom wall are  $\psi_{bottom} = -(U_0 + t^m)H$ ; also  $u = 0$ ,  $v = 0$ . At the outlet, we have used the zero gradient boundary condition  $\frac{\partial \psi}{\partial x} = \frac{\partial u}{\partial x} = \frac{\partial v}{\partial x} = 0$ .

It is worth mentioning that since we are using a Cartesian grid for discretizing the governing equations, the grid must be generated in such a way that the wedge geometry passes through the nodes. This was accomplished in the following way. Firstly, a square block is created in the domain  $-l \leq x \leq l$ ,  $0 \leq y \leq 0.5$ , where the value of  $l$  depends on the wedge angle. Along  $y$ -direction, a centro-symmetric grid with clustering at the top and bottom is generated

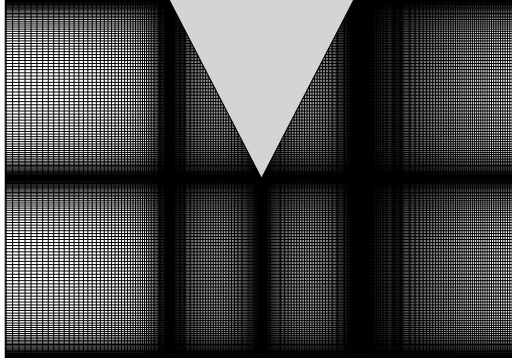


Figure 4: Schematic of the overall grid used for the accelerated flow past an wedge mounted on wall.

using the stretching function

$$y_j = \frac{j}{j_{max}} - \frac{\lambda}{2\pi} \sin\left(\frac{2\pi j}{j_{max}}\right), \quad 0 < \lambda \leq 1 \quad (3.3)$$

with  $\lambda$  determining the intensity of clustering (we used  $\lambda = 0.4$  here). Then in the sub-domain  $0 \leq x \leq l$ ,  $0 \leq y \leq 0.5$ , the grid along the  $x$ -direction is generated using the transformation  $x = (\tan \theta)y$ , where  $\theta$  is the wedge-angle (figure 3(a)). The grid in the sub-domain  $-l \leq x \leq 0$ ,  $0 \leq y \leq 0.5$  is obtained by creating a mirror image of the grid in the sub-domain  $0 \leq x \leq l$ ,  $0 \leq y \leq 0.5$  about the vertical line  $x = 0$ . This completes the generation of grid in the fundamental block (figure 3(b)) which accommodates the wedge geometry to pass through the grid points (figure 3(c)). Following this, the two neighbouring blocks on the left and right of it (see figure 4) are generated using nonuniform grid spacing in the  $x$ -direction where points are clustered in the neighbourhoods of the vertical boundaries of the fundamental block. This completes the grid in the domain  $-6.0 \leq x \leq 6.0$ ,  $0 \leq y \leq 0.5$ . The grid in the domain  $-6.0 \leq x \leq 6.0$ ,  $-0.5 \leq y \leq 0$  is an exact replica of the previous grid just above it as shown in figure 4. Thus the grid generation in the whole computational domain is complete. During the entire process, care must be taken such that the continuity of the grid lines in either direction of the whole computational domain is maintained. Note that grid points around the neighbourhoods of the three vertices of the triangle defining the wedge are extremely clustered. We performed computations on grids of sizes  $401 \times 101$ ,  $641 \times 161$ ,  $801 \times 201$  and  $1201 \times 301$  for channel Reynolds numbers 1560, 6621, and 6873, which correspond to  $m = 0$ ,  $m = 0.45$ , and 0.88 respectively. In the process, we also carry out a grid-convergence study of our computed results. For this, we present the horizontal and vertical velocities ( $u$  and  $v$ ) along the vertical line at  $x = 0.3$  on all the four different grids used in computation, viz.,  $401 \times 101$ ,  $641 \times 161$ ,  $801 \times 201$  and  $1201 \times 301$  for  $Re_c = 6873$  at three different instants of non-dimensional time  $t = 0.3$ , 0.6 and 0.75 in figure 5. For the first three grid, a time step  $\Delta t = 10^{-5}$  was used, while for the last  $\Delta t = 5 \times 10^{-6}$  was chosen. These figures clearly demonstrate the grid-independence of our computed solutions. Note that for all the numerical results that follow, a grid of size  $801 \times 201$  with  $\Delta t = 10^{-5}$  has been used for  $Re_c = 1560$  and 6621. For  $Re_c = 6873$ , the results presented here were computed on a grid of size  $1201 \times 301$  with  $\Delta t = 5 \times 10^{-6}$ .

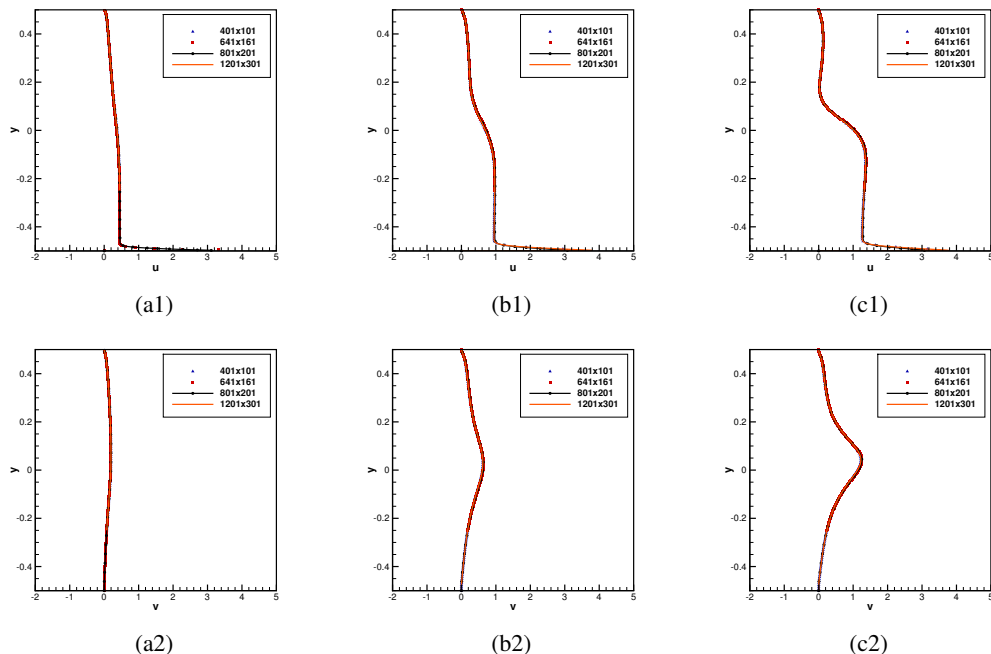


Figure 5: Grid independence of the computed solutions for four different grids at three different time step:  $u$  (top) and  $v$  (bottom) along the vertical line at  $x = 0.3$  at times (a1,a2)  $t = 0.3$ , (b1,b2)  $t = 0.6$  and (c1,c2)  $t = 0.75$  for  $Re_c = 6873$ .

## 4. Results and Discussion

As mentioned earlier, the current work is inspired by the experimental visualizations reported by Pullin and Perry (1980) in their start-stop lab experiments, which we would endeavour to replicate through numerical simulation. Note that, in their experiments, the flow was stopped at actual times as shown in table 1, whose corresponding non-dimensional time  $t < 1$  Pullin and Perry (1980). However, we continued our simulations up to a non-dimensional time  $t = 3.0$  to delve into the flow beyond the experimental visualization of Pullin and Perry (1980) and have a better understanding of the flow characteristics.

### 4.1. Flow development at the earliest stage

In figures 6(a)-(h) and 7(a)-(h), one can see the earliest stages of flow development for  $Re_c = 6873$ . While figure 6 demonstrates the streamlines and their close-up views, figure 7 depicts the corresponding vorticity contours. Here, all the four stages of start-up vortex evolution, reported by Xu and Nitsche (2015), Xu (2016) and Koumoutsakos and Shiels (1996) can be observed clearly; however, the flow evolution for the wedge subjected to accelerated flow is much more rapid than the one observed in the accelerated flat plate case (Xu and Nitsche (2015); Koumoutsakos and Shiels (1996)). Initially, the formation of an almost symmetrical vortex is observed at the tip of the wedge (can be seen at  $t = 0.01$  in figures 6(a), 6(e), 7(a) and 7(e)) with a boundary layer of uniform thickness around it. All the vorticity values are positive at this juncture, with the highest value appearing at the wedge tip. Vorticity contours then start deviating towards the leeward direction, still without any separating streamline (with value  $\psi = 0$ ). This is the Rayleigh stage, duration of which ends when a negative vorticity region forms within the starting vortex near the wedge wall with a well-defined center of rotation and bounding streamline as seen in figures 6(b), 6(f),

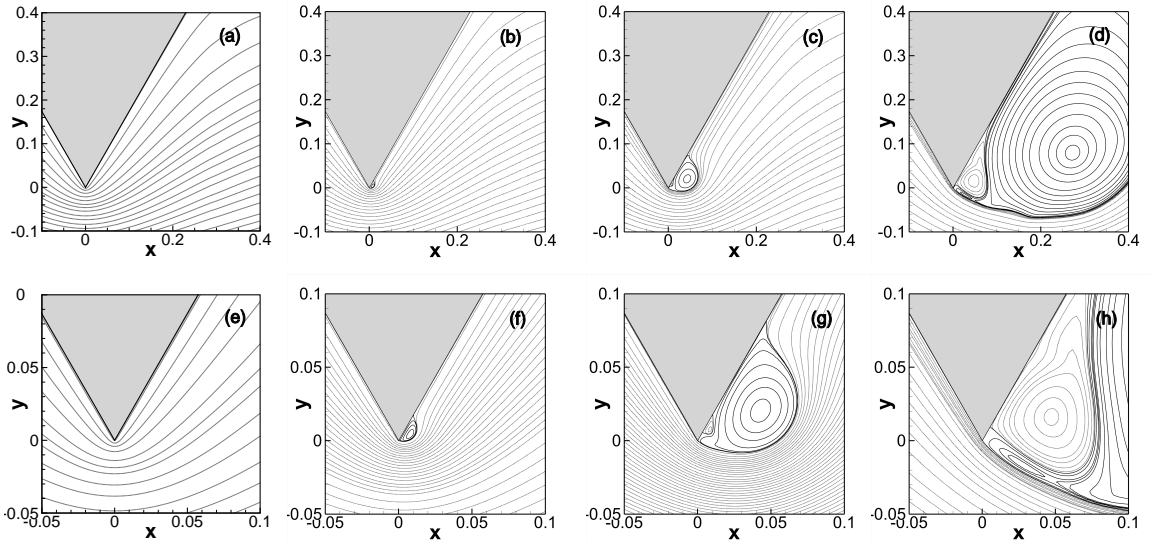


Figure 6: Four stages of streamfunction evolution for  $Re_c = 6873$  at non-dimensional time (a)  $t = 0.01$ , (b)  $t = 0.10$ , (c)  $t = 0.30$  and (d)  $t = 1.0$ , and the corresponding close-up views in (e-h). The positive contours are in solid lines and negative contours are in dotted lines.

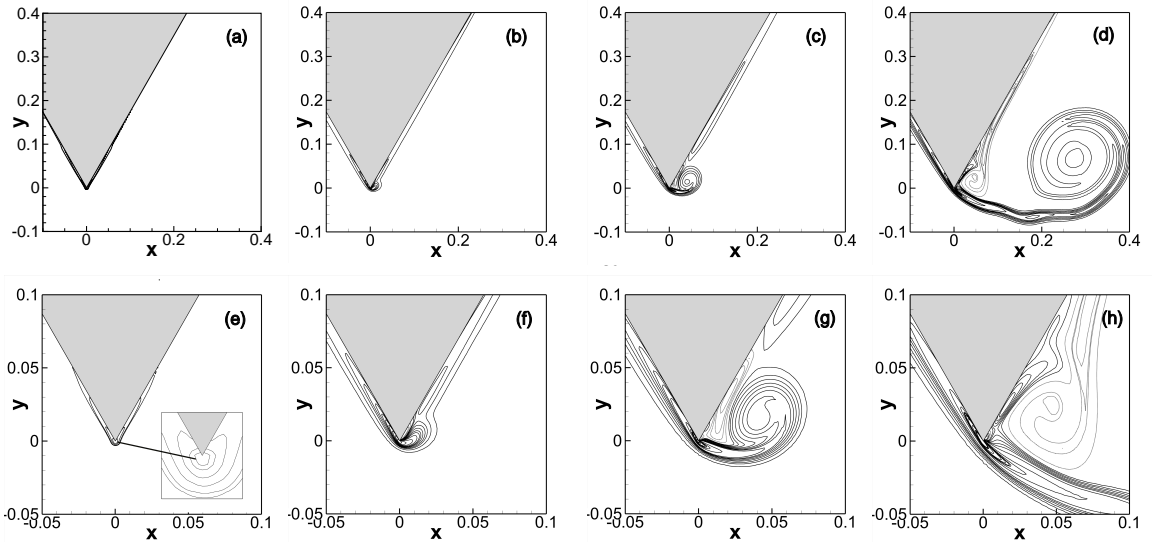


Figure 7: Four stages of vorticity evolution for  $Re_c = 6873$  at non-dimensional time (a)  $t = 0.01$ , (b)  $t = 0.10$ , (c)  $t = 0.30$  and (d)  $t = 1.0$ , and the corresponding close-up views in (e-h). The positive contours are in solid lines and negative contours are in dotted lines.

7(b) and 7(f) at time  $t = 0.10$ . This is the Viscous stage where the convective terms of the N-S equations become comparable with the viscous terms and thus the well-defined vortex structures begin to appear. As time passes, the negative vorticity boundary layer thickens, causing the starting vortex to separate from the wedge. After a while, the vorticity acquires a local maximum in the vortex core as seen in figures 6(c), 6(g), 7(c) and 7(g) at time  $t = 0.3$ ,

which was not observed in figures 6(b), 6(f), 7(b) and 7(f). This is the self-similar inviscid stage. At this stage, convective terms become dominant, but the vortex is still small enough to be independent of the geometry except for the local edges. Eventually the outer streamline detaches from the slant wedge wall giving rise to the stage known as vortex expulsion. The initial recirculation bubble opens up, freeing it up from the self-similar growth and the vortex starts lagging behind the body as shown in (figures 6(d), 6(h), 7(d) and 7(h) at time  $t = 1.0$ ). The starting vortex grows in size and is convected downstream, which in turns induces a secondary vortex at the tip of the wedge as can be seen in figure 6(g). The orientation of flow inside this secondary vortex is in the direction opposite to the primary one.

It would be interesting to see approximately at what time flow separates from the wedge wall giving rise to the vortex phenomena mentioned above. It is well known that whenever vorticity changes sign along a solid wall, flow separation takes place paving the way for the creation of a vortex (Anderson Jr (1995); Pletcher et al. (2012); Kalita and Sen (2013)). As such, the number of vortices will depend upon the total number of changes of sign in vorticity values. We illustrate this phenomenon in figures 8(a)-(f). In figures 8(a), (c) and (e), we have plotted the vorticity distribution against the  $x$ -coordinate of the wedge wall and different times, while figures 8(b), (f) and (f) depicts the corresponding combined streamfunction and vorticity contours. In figure 8(a), one can clearly see that at time  $t = 0.02$ , there is no change of sign of vorticity along the wall, similar to the situation depicted in figure 7(e) at time  $t = 0.01$ . On the other hand, at a later time  $t = 0.06$ , one can see a very small zone of negative vorticity value which corresponds to the white region in figure 8(b), enclosed by the (primary) vortex bounded by the  $\psi = 0$  streamline. This clearly demonstrates that the first flow separation takes place in the interval  $t \in (0.02, 0.06]$ . Likewise, in figure 8(c), one can see that at  $t = 0.20$ , there is only one negative vorticity zone across the wedge wall. However, at  $t = 0.25$ , one can see a very narrow zone of positive vorticity inside the primary vortex zone (see the enlarged view in the inset), giving rise to the second separation. This secondary vortex can be seen more clearly in figure 8(d), where the region in green colour is enclosed by the  $\psi = 0$  streamline and the primary vortex that engulfs the secondary vortex is represented by the white region (see also figures 6(g) and 7(g) at time  $t = 0.30$ ). This indicates a second flow separation in the interval  $t \in (0.20, 0.25]$ . Meanwhile, the secondary vortex grows in size and strength and at around  $t = 0.6$  divides the primary vortex into two chambers, one of which is the core and the other one gives rise to a tertiary recirculating zone. It becomes more prominent at  $t = 0.90$  onwards, which can also be observed in figures 6(d) and (h). The vorticity distribution along the wall in figure 8(c) at  $t = 0.90$  clearly demonstrates these three primary, secondary and tertiary recirculation zones, with figure 8(f) showing the small negative vorticity region in the neighbourhood of the wedge-tip.

#### 4.2. Movement of the primary vortex center and the $m$ effect

In their laboratory experiment, Pullin and Perry (1980) presented the trajectories of the primary vortex center obtained directly from the measured frame by frame projection of their cine film. In the absence of any vorticity measurement in their experiments, they had taken the approximate geometric center, or the center of flow rotation of the vortex streaklines as the vortex center. Following Xu and Nitsche (2015); Xu (2016), we also define the vortex center  $(x_M, y_M)$  as the point in the computational domain having local vorticity maximum  $\omega_M$ . On the other hand, we define the rotation center  $(x_R, y_R)$  as the point having local streamfunction maximum and denote the vorticity thereat as  $\omega_R$ . The schematic of the vortex and rotation centers are depicted in figure 9, where the thick curves in black represent the streamlines and the red curves the vorticity contours. In figures 10(a)-(c), we show the trajectories of these vortex and rotation centers for  $Re_c = 1560$ ,  $Re_c = 6621$  and  $Re_c = 6873$  respectively. Note that, while a well defined rotation center is observed immediately after the

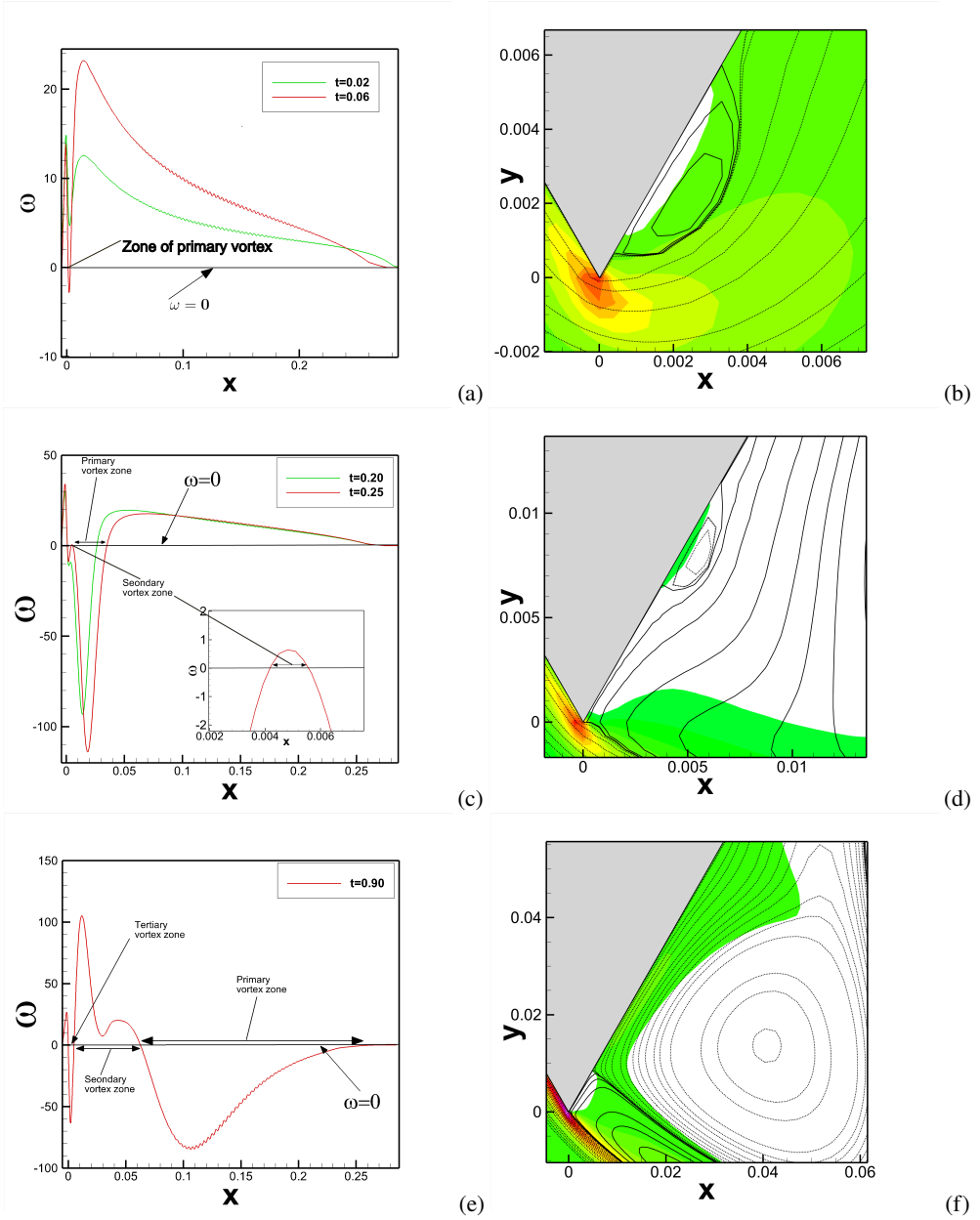


Figure 8: Flow separation from the wedge wall for  $Re_c = 6873$ : Distribution of vorticity along the wedge wall at time (a)  $t = 0.02$  &  $t = 0.06$ , (c)  $t = 0.20$  &  $t = 0.25$  and (e)  $t = 0.90$ . Combined streamfunction (dotted lines representing negative values and solid lines representing positive values) and vorticity contours (flooded, white colour representing areas with negative values) at time (b)  $t = 0.06$ , (d)  $t = 0.25$  and  $t = 0.90$ .

first separation as documented in section 4.1, it takes a while for the local maximum vorticity to set in and hence the formation of a well-defined vortex center. Our computation reveals that the first appearance of local vorticity maximums for  $Re_c = 1560$ ,  $Re_c = 6621$ ,  $Re_c = 6873$  occurred at instants  $t = 0.05$ ,  $t = 0.08$  and  $t = 0.2$  respectively. At those respective instants,



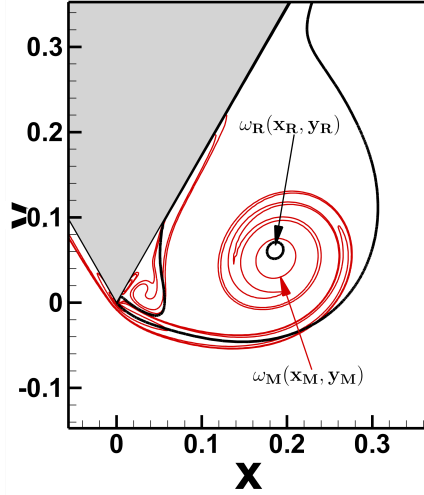


Figure 9: Schematic of vortex and rotation centers. The vortex center lies inside the small red circular shape and the rotation center, inside the black one, as marked by the arrows.

the locations of the rotation and vortex centers are much closer to the wedge-tip for  $m \neq 0$  than for the uniform flow as can be seen from figures 10(a)-(c).

For the initial part ( $t \leq 1$ ), when the rolled-up vortex is almost self similar, the trajectories almost moves in a straight line and the vortex center is always below the rotation center. However, with the onset of shear layer instability (see section), for  $t > 1$ , their movement becomes more dispersed and rapid.

The effect the parameter  $m$  on the trajectories of vortex centers may be interpreted in terms of the movement of the wedge driven by the piston depicted in figure 1. If the wedge is moved from rest in the horizontal direction with a non-dimensional driving velocity obeying  $u_d = t^m$ , it will traverse a distance

$$d = \frac{t^{m+1}}{m+1}. \quad (4.1)$$

In figures 11(a)-(b), we plot the graphs of non-dimensional driving velocity  $u_d$  and distance  $d$  as a function of the non-dimensional time  $t$  respectively. The solution at a fixed time depends on  $m$ , as the wedge would have traversed significantly different distances  $d$  for different values of  $m$  as the formula suggests. It is obvious from the expressions for  $u_d$  and  $d$  that for  $t \leq 1$ ,  $u_d$  is a decreasing function of  $m$ , while for  $t > 1$ , it is the opposite scenario. The same can be said about  $d$  for approximately  $t \leq 2$  and  $t > 2$ . This explains the rapid movement of vortex centers away from the wedge tip for  $t > 2$  when  $m \neq 0$  (figures 10(b)-(c)), with farthest displacement occurring for  $m = 0.88$ , the largest value of  $m$  considered in this study.

The effect of  $m$  is further displayed in figures 12 and 13 depicting the streamlines for the three values of  $m$  considered at times  $t = 0.8$  and  $t = 2.0$  respectively. Note that the displacement of the primary vortex center away from the wedge-tip is related to its growth as well. In figure 12 one can observe that with increase in  $m$ , the size of primary vortex is



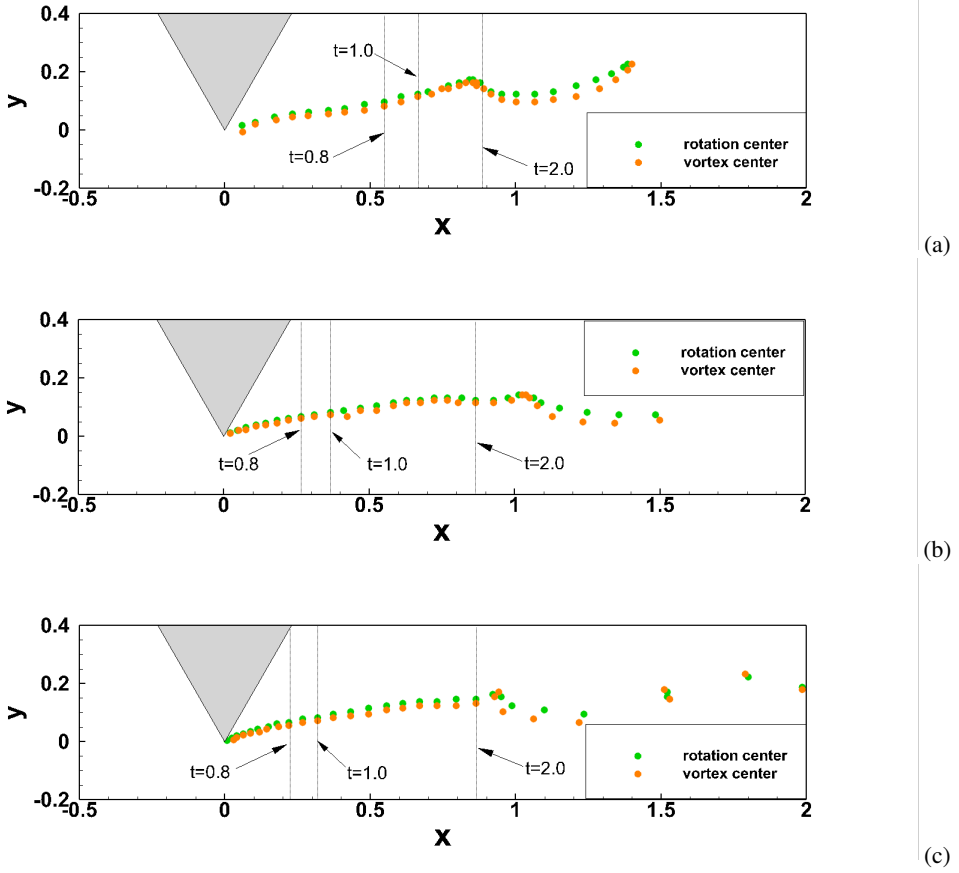


Figure 10: Vortex and rotation center trajectories during  $0 < t \leq 3.0$  for (a)  $Re_c = 1560$  ( $m = 0$ ), (b)  $Re_c = 6621$  ( $m = 0.45$ ) and (c)  $Re_c = 6873$  ( $m = 0.88$ ).

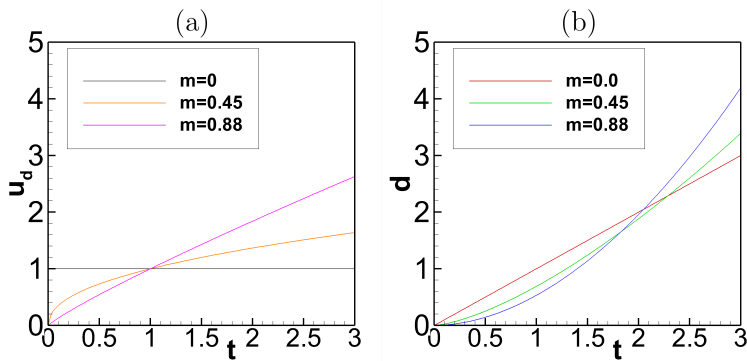


Figure 11: Effect of  $m$  on non-dimensional driving velocity and distance: (a)  $u_d$  against  $t$  and (b)  $d$  against  $t$ .

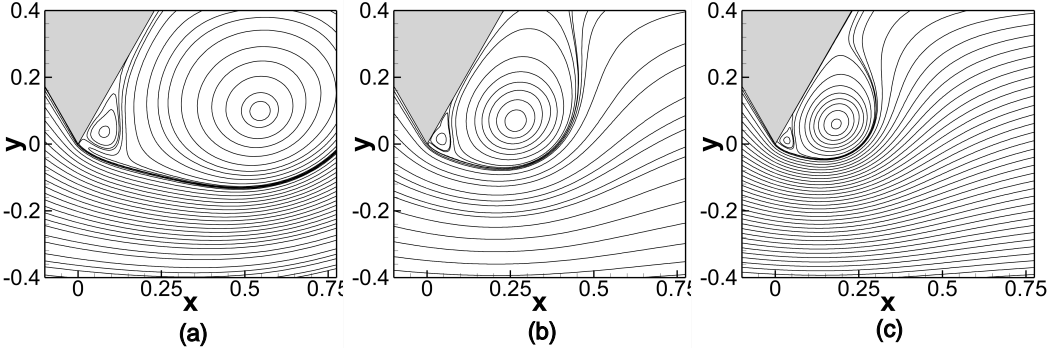


Figure 12: Streamlines for accelerated flow past a  $60^\circ$  wedge at time  $t = 0.8$  for (a)  $Re_c = 1560$  ( $m = 0$ ), (b)  $Re_c = 6621$  ( $m = 0.45$ ) and (c)  $Re_c = 6873$  ( $m = 0.88$ ).

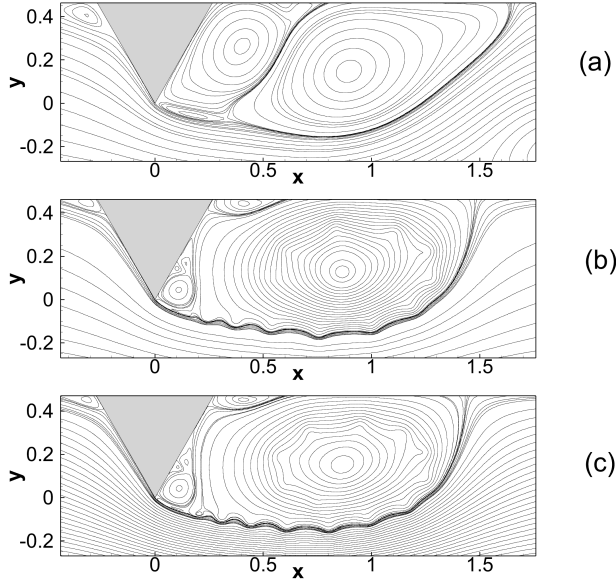


Figure 13: Streamlines for accelerated flow past a  $60^\circ$  wedge at time  $t = 2.0$  for (a)  $Re_c = 1560$  ( $m = 0$ ), (b)  $Re_c = 6621$  ( $m = 0.45$ ) and (c)  $Re_c = 6873$  ( $m = 0.88$ ).

reducing. This is because of the fact that both  $u_d$  and  $d$  are decreasing functions of  $m$  for  $t \leq 1$ . As such, till time  $t = 1.0$ , a stronger velocity field is indicated for  $m = 0$  which is also obvious from figure 11(a). On the other hand, as seen from figure 11(b), from around  $t = 2.0$ , the distances corresponding to  $m \neq 0$  overtakes the ones for  $m = 0$ . This is the reason one can see the displacement of vortex centers and the size of the primary vortices almost catching up with each other as in figures 13(a)-(c) and 10(a)-(c), where the location of the vortex centers are marked at times  $t = 0.8$  and  $t = 2.0$  as well. This exemplifies the role of the parameter  $m$  above.

Next, we look at the flow for a fixed displacement  $d$  of the wedge for varying  $m$ 's, which provides a better understanding of the whole phenomena (Xu and Nitsche (2015)). In figure 14, we compare the vorticity contours, streaklines and the streamlines for a fixed displacement  $d = 1$  of the wedge for  $m = 0, 0.45$  and  $0.88$  (see table 2 also). The corresponding vector field in the vicinity of the tip of the wedge is shown in figure 15. One can again observe

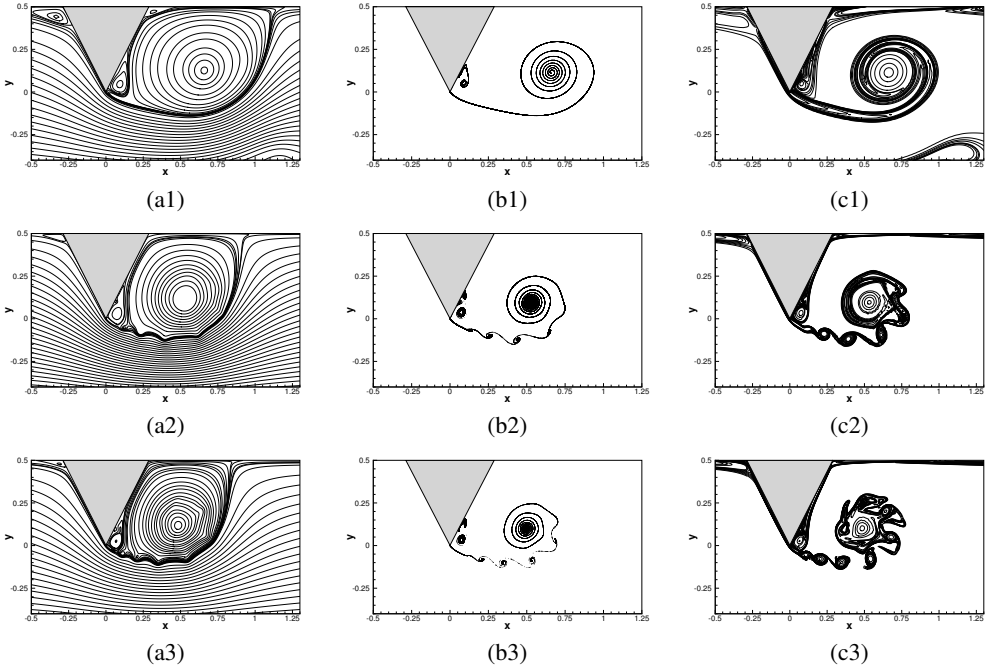


Figure 14: Effect of  $m$  on the flow field for a fixed displacement  $d = 1$ : The rows from the top to the bottom correspond to  $m = 0, 0.45$  and  $0.88$  and the columns represent (a1-a3) Streamfunction, (b1-b3) streaklines and (c1-c3) vorticity for  $Re_c = 1560$  (top row),  $Re_c = 6621$  (middle row) and  $Re_c = 6873$  (bottom row).

gradual decrease in the size of the vortices for the early part of the flow from figures 14(a1)-(a3) with increase in  $m$ . The development of shear layer is more prominent as  $m$  increases, which is also obvious from the velocity vector plots in figures 15(a)-(c). The density of the streamlines below the bounding streamline of the core vortex indicates a stronger velocity field with increase in  $m$ , which is also reflected by the length of the vectors. The streaklines and vorticity contours in figures 14(b2)-(b3) and 14(c2)-(c3) clearly demonstrate that for the accelerated flow, shear layer instability has set in, which is indicated by the waviness of the outermost vortex layer of the starting vortex (see figures 13(b)-(c) and 15(b)-(c) also). This will be discussed in more details in the next section. In figure 16, we show the vorticity profile as a function of zero and non-zero values of  $m$  which corresponds to the wedge experiencing a uniform and accelerated flow respectively. Here we plot the vorticity values corresponding to  $m = 0$  and  $0.88$ , and  $d = 1$  along the horizontal line passing through the core vortex center. One can clearly see larger maximal vorticity occurring for smaller value of  $x$  for non-zero  $m$ , reflecting the smaller shape of the vortices for the accelerated flow. The shear layer instability for the accelerated case is clearly indicated by the highly oscillating nature of the graph against a much well-behaved one for the uniform flow case.

It must be mentioned that the flow evolution in terms of the non-dimensional variables may portray a slightly different scenario than the real time flow field evolution. This is because of the fact that except displacement, for each of the other flow variables, a non-linear scaling (see equation (2.3)) has been used. Therefore, though figure 13 reveals the proximity of the horizontal distances traversed by the vortex centers for a fixed non-dimensional time  $t = 2.0$ , in reality, when the flow is devoid of any acceleration, the time taken for the same is approximately four times than when it is subjected to acceleration. This fact is also revealed

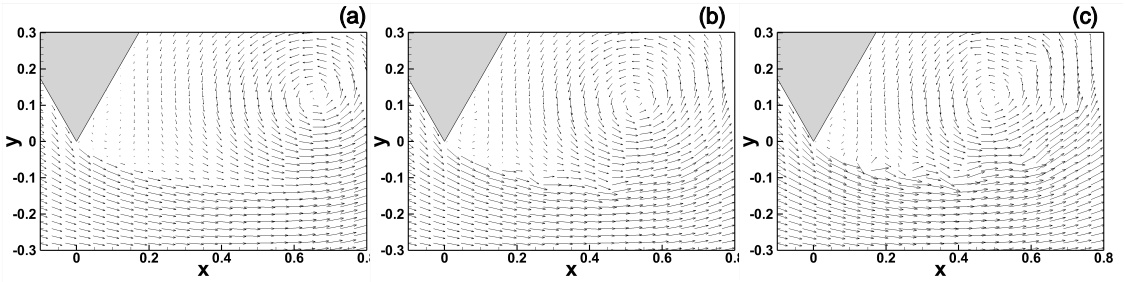


Figure 15: The vector field close to the wedge tip for  $d = 1$  and (a)  $Re_c = 1560$ , (b)  $Re_c = 6621$  and (c)  $Re_c = 6873$ .

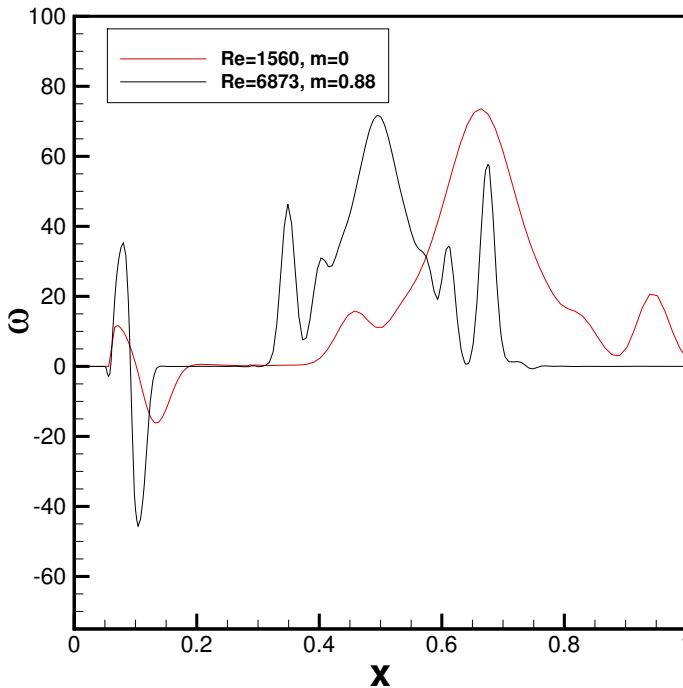


Figure 16: Vorticity distribution across the horizontal line through the core vortex center for  $d = 1$ : (a)  $Re_c = 1560$  and (b)  $Re_c = 6873$ .

by table 2, where we have tabulated the horizontal coordinate  $x_R$  of the rotation center at fixed non-dimensional times  $t = 0.8$  and  $t = 2.0$  along with their corresponding physical times. Also tabulated here are the dimensional and non-dimensional times against a fixed distance  $d = 1$  (or a physical distance  $\bar{d} = 25.4cm$ , see figure 14 also), which reveals a similar trend. It further reasserts that acceleration in the flow triggers shear layer instability early in the flow (around real time 13 *secs*), while no trace of such instability is seen for uniform flow even after 80 *secs*.

The effect of non-dimensionalization on the flow could also be understood from the formula for distance  $d$  traversed by the wedge calculated in terms of the non-dimensional time  $t$  as in

Table 2: Effect of non-dimensionalization on the flow field.

	m	0	0.45	0.88
t=0.8	$x_R$	0.549	0.266	0.180
	$\tilde{t}$ (in sec)	32.25	8.26	7.48
t=2.0	$x_R$	0.890	0.866	0.865
	$\tilde{t}$ (in sec)	80.64	20.66	18.70
d=1.0	t	1.0	1.29	1.40
	$\tilde{t}$ (in sec)	40.32	13.34	13.08

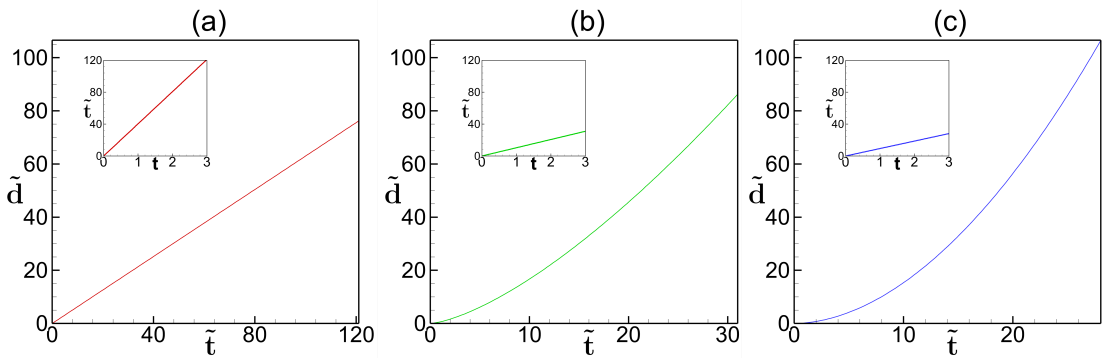


Figure 17: Effect of non-dimensionalization on flow visualization, actual distance travelled in real physical time, with non-dimensional time versus the real time at the inset for: (a)  $Re_c = 1560$  ( $m = 0$ ), (b)  $Re_c = 6621$  ( $m = 0.45$ ) and (c)  $Re_c = 6873$  ( $m = 0.88$ ). The units of  $\tilde{t}$  and  $\tilde{d}$  are in *sec* and *cm* respectively.

equation (4.1) above, which will translate into  $\tilde{d} = A \frac{\tilde{t}^{m+1}}{m+1} cm$  in real physical time. This is actually the distance traversed by the piston in the laboratory experiment of Pullin and Perry (1980). For the benefit of the readers, we also plot these actual distances (in *cm*) the piston would have travelled in real physical time (in *sec*), with non-dimensional time versus the real time at the inset corresponding to these  $m$  values in figures 17(a)-(c). These figures, along with the backdrop of the non-dimensional distances plotted in figure 11(b) clearly reveal the contrasts between the actual distance travelled against the non-dimensional ones.

#### 4.3. Numerical simulations vis a vis Experimental visualization: the earliest stage of flow evolution

In the next figures 18-19, we present the the earliest stage of flow evolution respresented by streaklines from the experimental visualization of Pullin and Perry (1980) side by side with from the ones from our simulation along with the corresponding streamlines and vorticity contours for  $Re_c = 1560$  and  $6873$  respectively. The flow characteristics for  $Re_c = 6621$  is almost similar to that of  $Re_c = 6873$  and hence not compared here. For the streamlines and vorticity contours, solid lines represent positive and dotted ones negative values of the contours. It is observed that the start up vortex for  $Re_c = 1560$  performs more rounds of

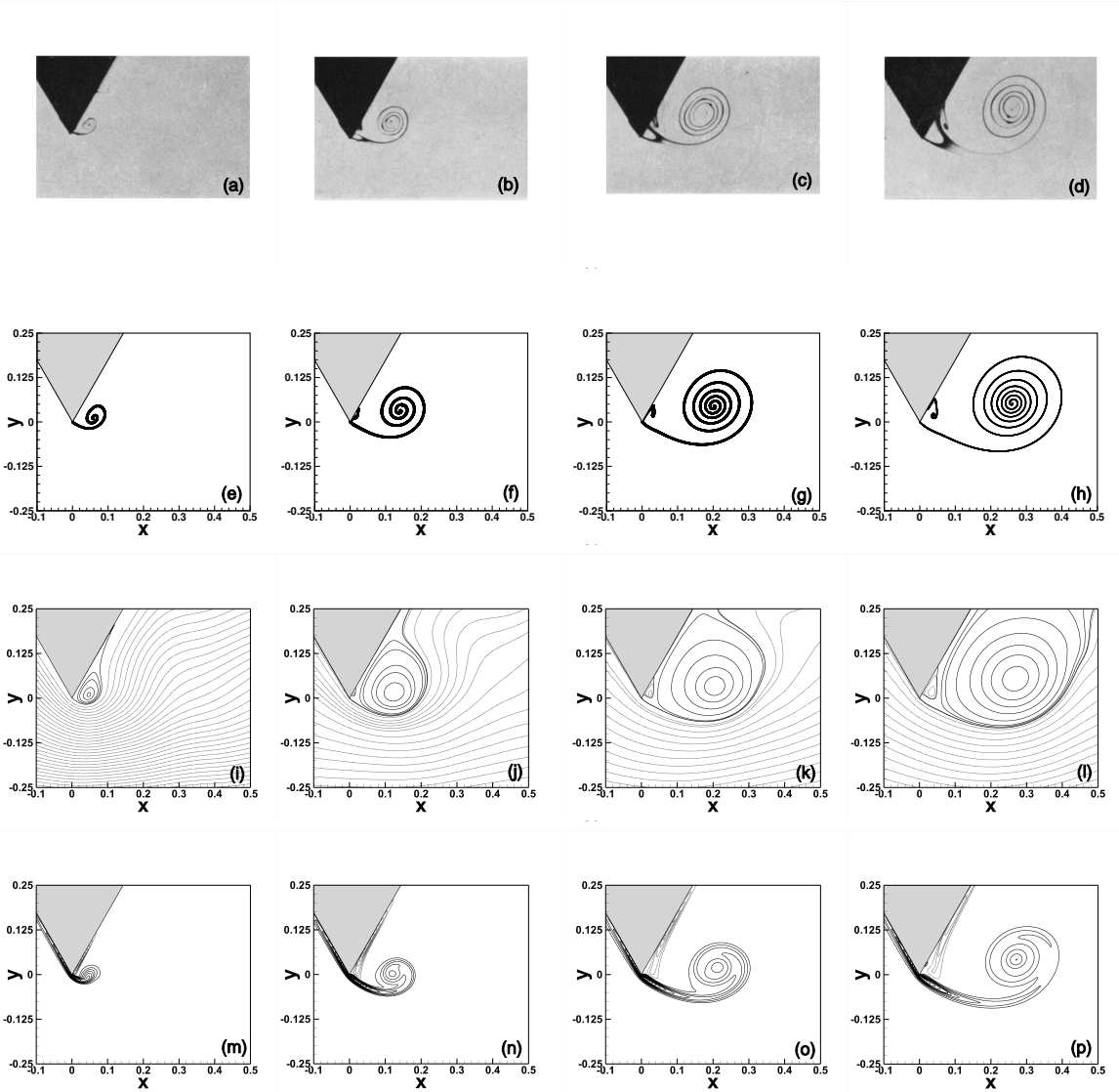


Figure 18: *Streaklines from experimental visualization of Pullin and Perry (1980) (a-d) and our computation (e-h) and the corresponding streamlines (i-l) and vorticity contours (m-p) the for flow past a wedge for  $Re_c = 1560$  and  $m = 0$  at instants  $\tilde{t} = 1$  sec ( $t = 0.024803$ ),  $\tilde{t} = 3$  sec ( $t = 0.074409$ ),  $\tilde{t} = 5$  sec ( $t = 0.124016$ ) and  $\tilde{t} = 7$  sec ( $t = 0.173622$ ).*

rotations at time  $\tilde{t} = 7$  sec than  $Re_c = 6873$  as can be seen from the extreme right columns of figures 18 and 19, indicating a stronger circulation for the former in the early stage of the flow. Moreover, the secondary vortex phenomena is more prominent for  $Re_c = 6873$  than  $Re_c = 1560$ .

It is heartening to see that our computed results are extremely close to the experimental results of Pullin and Perry (1980). The locations of the primary and the secondary vortex centers, their size and shape, and precise instants of their occurrence bear testimonial to the accuracy in capturing the attributes of the fluid flow. Apart from the computational accuracy

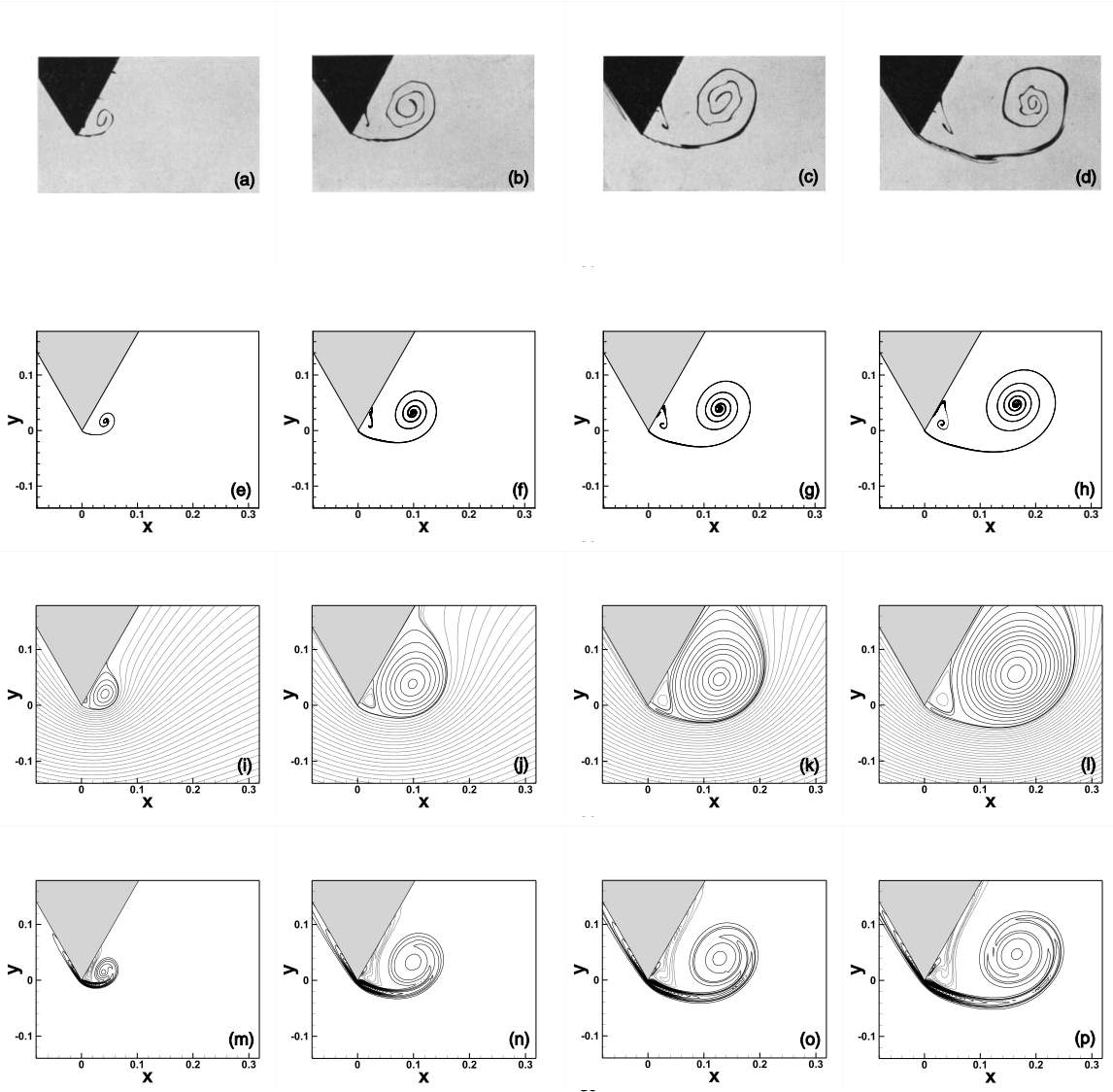


Figure 19: Streaklines from Pullin and Perry's experimental visualization (a-d) and our computation (e-h) and the corresponding streamlines (i-l) and vorticity contours (m-p) the for flow past a wedge for  $Re_c = 6873$  and  $m = 0.88$  at instants  $\tilde{t} = 2.8$  sec ( $t = 0.299493$ ),  $\tilde{t} = 5$  sec ( $t = 0.534809$ ),  $\tilde{t} = 6$  sec ( $t = 0.641771$ ) and  $\tilde{t} = 7$  sec ( $t = 0.748733$ ).

of the data, this example also aptly demonstrates the capacity of the scheme developed by the authors (Kumar and Kalita (2020)) in handling both Dirichlet and Neumann boundary conditions with equal ease. A close look at the boundary conditions mentioned in section 3 would reveal that while Dirichlet boundary conditions have been used for  $\psi$  at the top and bottom walls, inlet and on the surface of the wedge, Neumann boundary condition has been employed at the outlet. It is worth mentioning that while we have used exact physical boundary conditions matching the ones used in the lab experiment of Pullin and Perry (1980), in their flow simulations, Xu and Nitsche (2015); Xu (2016) used potential flow conditions

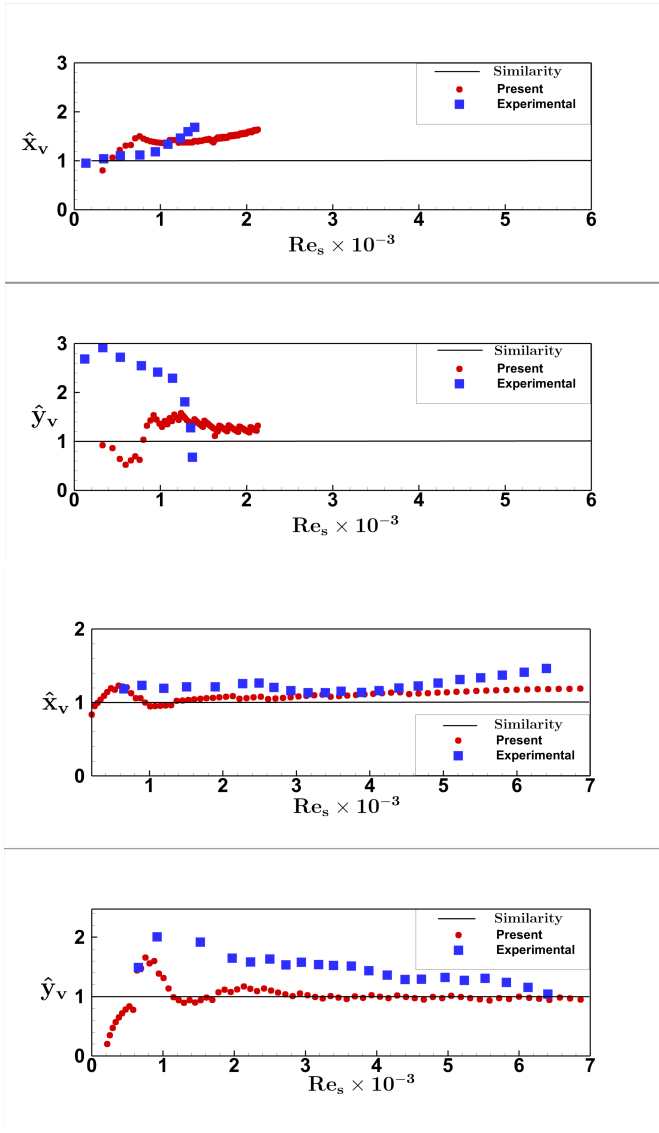


Figure 20: Comparison of experimental (Pullin and Perry (1980)) and numerical vortex center movements with the similarity solutions for (a)  $Re_c = 1560$  and (b)  $Re_c = 6873$ .

in the far field equivalent to considering an infinite wedge (or flat plate immersed in viscous fluid contained in an unconfined domain).

#### 4.4. Inviscid scaling

Pullin and Perry (1980) also compared the movement of the vortex centers resulting from their laboratory experiments with that of the rolled up vortex-sheet model found from the scaling laws of Pullin's earlier numerical work on the starting flow past an infinite wedge (Pullin (1978)). The initial trajectory of the vortex-centers of these self-similar structures in dimensionless form was given by



$$\hat{x}_v = \frac{\tilde{x}_M}{a^{1/(2-n)} \tilde{t}^M \mathcal{R}}, \quad \hat{y}_v = \frac{\tilde{y}_M}{a^{1/(2-n)} \tilde{t}^M \mathcal{I}} \quad (4.2)$$

where  $a = \alpha_0 A H^{1-n}$ , with  $\alpha_0$ ,  $n$ ,  $A$  and  $H$  are as defined in (2.3) and (2.5), and  $\mathcal{R}$ ,  $\mathcal{I}$  represent the real and imaginary parts of a complex argument that can be found from table 2 of Pullin and Perry (1980). Using the length and time scales defined in equation (2.3), (4.2) reduces to

$$\hat{x}_v = \frac{x_M}{\alpha_0^{1/(2-n)} t^M \mathcal{R}}, \quad \hat{y}_v = \frac{y_M}{\alpha_0^{1/(2-n)} t^M \mathcal{I}} \quad (4.3)$$

where  $(x_M, y_M)$  is the coordinate of the vortex center defined in section 4.2.

In figure 20, we present the scaled values of the coordinates of the primary vortex center, or in other words, the horizontal and vertical displacements of the vortex centers from the wedge-tip as a function of the scale Reynolds number  $Re_s(t)$  defined by (2.6) and compare them with the experimental results of Pullin and Perry (1980) as well as the inviscid similarity theory proposed by Kaden (1931). As  $Re_s$  increases, one can clearly see more deviation of the vortex centers from the similarity solutions, more so, for  $\hat{x}_v$ . Pullin and Perry (1980) attributed this break-down of similarity behaviour to the influence of the channel boundaries and three-dimensional effect. One can see from figure 20(a), for the uniform flow ( $Re_c = 1560$ ), our results deviates a bit from the experimental results as had been observed in Xu (2016) as well. However, our results are relatively closer to the experimental ones than theirs. On the other hand, for the accelerated case for  $Re_c = 6873$ , our computed solutions are much closer to the experimental observations, and follow the similarity solutions very closely.

#### 4.5. The Structure of Vortex shedding beyond the experimental visualization of (Pullin and Perry 1980)

In this section, we provide a detailed description of different stages of evolution for the flow past a wedge mounted on a wall subjected to accelerated flow for  $Re_c = 6873$  until transition to turbulence. Note that Pullin and Perry (1980) continued their laboratory experiment only up to a non-dimensional time  $t \approx 0.76$  in their study, while we carried out our numerical experiment for the same up to  $t = 3.10$ . In the absence of any experimental visualisation beyond  $t = 0.76$  for this flow configuration, we relied on the experimental visualisation of Lian and Huang (1989), who conducted a series of experiments for the flow past flat plates with sharp edges in the range  $2000 \leq Re \leq 15000$ , to compare our computed results. They used hydrogen bubble technique to visualize the flow and reported three stages of evolution of the starting vortices culminating in a three-fold structure leading to the onset of transition to turbulence. Our investigation also revealed that all these three stages are very much evident during the course of the flow which we detail here. Note that since Lian and Huang (1989) provided pictures only for the upper edge of the plate, in some of the figures that follow next, their experimental visualization pictures have been tilted upside down to compare our results with theirs.

##### 4.5.1. Initial Stage

The spiral vortex sheet structure of the starting vortex is depicted in figures 21(a-c), where Lian and Huang (1989)'s experimental visualization in figure 21(a) is compared to the streaklines resulting from our computation in figure 21(b). The lead up to the formation of this vortex and its subsequent growth has already been discussed in section 4.1. The vortex shedding that originated from the edge has rolled up into a spiral shape with a densely wound-up core layer (see figures 19(a)-(h) also) (Pullin (1978)). The viscous effect causes the closely spaced shear layers in real fluids like the ones studied in these studies to combine

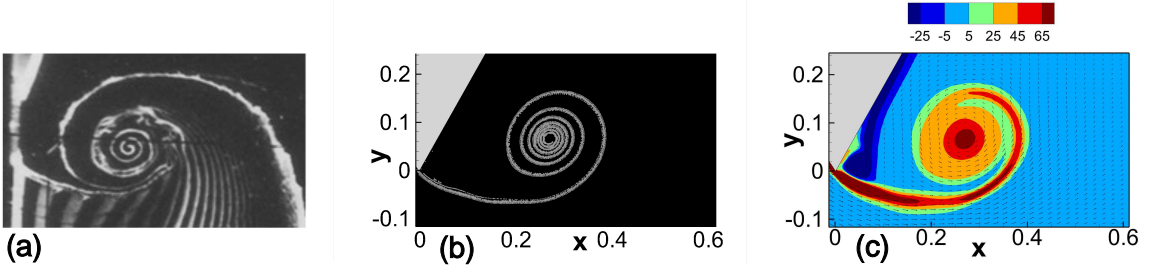


Figure 21: The initial stage: (a) Streaklines from the experimental result of Lian and Huang (1989) ( $t = 1.44$ ), (b) Streaklines from the present numerical computation for  $Re_c = 6873$  at  $\bar{t} = 9.35 \text{ sec}$  ( $t = 1.0$ ) and (c) Velocity vectors and vorticity contours from the present computation for  $Re_c = 6873$  at  $\bar{t} = 9.35 \text{ sec}$  ( $t = 1.0$ ).

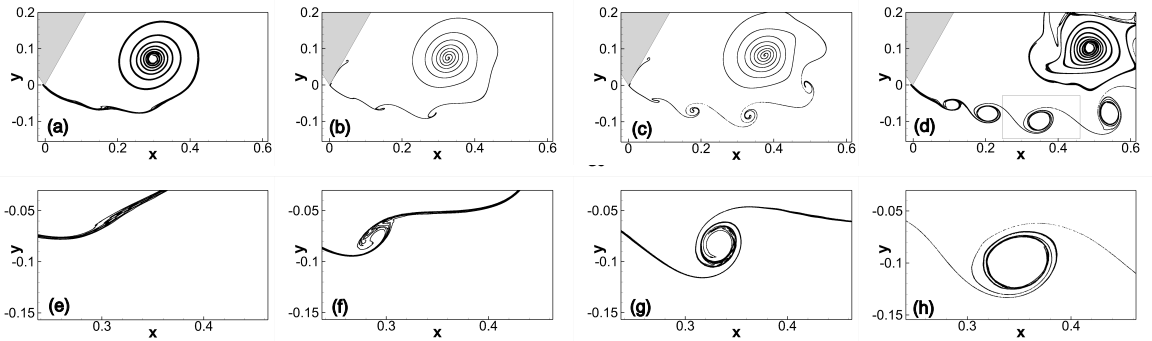


Figure 22: Onset of shear layer instability and beyond for  $Re_c = 6873$ : Streaklines at times (a)  $t = 1.06$  ( $\bar{t} = 9.91 \text{ sec}$ ), (b)  $t = 1.12$  ( $\bar{t} = 10.47 \text{ sec}$ ), (c)  $t = 1.20$  ( $\bar{t} = 11.22 \text{ sec}$ ) and (d)  $t = 1.40$  ( $\bar{t} = 13.09 \text{ sec}$ ). Close-up view of the evolution of double branching structure corresponding to the rectangular region in 22(d) above for the same instants.

swiftly into a rigid core, where the concentrated vorticity in the vortex sheet diffuses into uniformly distributed vorticity as can be seen in figure 21(a) and the velocity vectors and the flooded vorticity contours presented in figure 21(c).

#### 4.5.2. Second Stage

The second stage is fraught with the phenomenon of shear layer instability described earlier in section 4.1, which we depict in figure 22 where we have plotted streaklines near the wedge-tip at times  $t = 1.06$ ,  $1.12$ ,  $1.20$  and  $1.40$  along with their close-up views. Because of the shear layer instability, peripheral vortex layer of the starting vortex becomes wavy as can be seen from figure 22(a). Following that, a portion of peripheral layer of the vortex sheet splits and rolls up into little vortices, as depicted in figures 22(b)-(d). The starting vortex breaking into wavy structure is the announcement of shear layer instability and can be seen more clearly from figure 22(e)-(h), where we have shown close-up view of the streaklines corresponding to the region in the rectangular box of figure 22(d). These small vortices have a double-branched spiral roll structure as shown in figure 22(g)-(h), which is typical of shear layer instability (Tsai and Yue (1993)). In figure 23, we compare our computed streaklines at  $t = 2.0$  side by side with the experimental visualization of Lian and Huang (1989). The small vortex structures observed in this figure were also observed in the laboratory experiment of flow past an accelerated flat plate by Pierce (1961), and the numerical simulation of

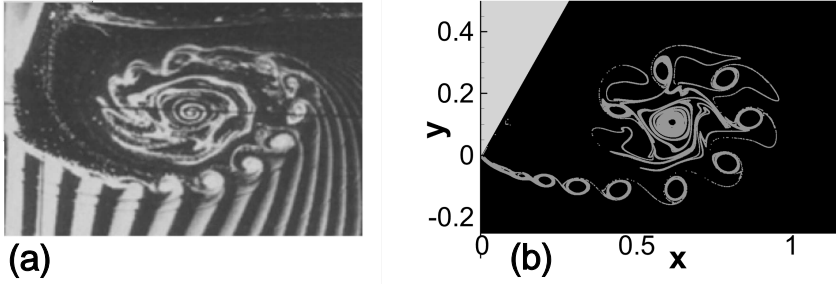


Figure 23: The second stage: Comparison of streaklines between (a) the experimental result of Lian and Huang (1989) ( $t = 2.09$ ) and (b) the present numerical simulation for  $Re_c = 6873$  at  $\tilde{t} = 14.95 \text{ sec}$  ( $t = 1.6$ ).

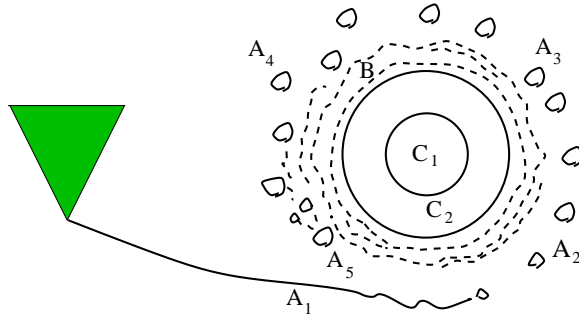


Figure 24: Schematic of the three-fold structure.

Koumoutsakos and Shiels (1996). One can clearly see from figures 23(a)-(b) that these small vortices are spaced almost uniformly, with their centers lying across the spiral curve of the the large starting vortex. This confirms that they are nothing but parts of the large starting vortex only. For a more vivid visual experience of the evolution of shear layer instability, one may look up the accompanying video "shear.avi".

#### 4.5.3. Third Stage: Three fold structure

Lian and Huang (1989) described this stage as the one marked by the existence of the three-fold structure. For the benefit of the readers, we re-enact the schematic of this typical structure of the starting vortex behind the wedge in figure 24. This stage is associated with the time frame  $t > 2$  depicted in figures 10(b)-(c) beyond the vertical line corresponding to  $t = 2.0$ . In figure 25, we have shown a comparison of streaklines between the experimental results of Lian and Huang (1989) ( $t = 2.885$ ) and the present numerical simulation for  $Re_c = 6873$  at  $\tilde{t} = 20.57 \text{ sec}$  ( $t = 2.2$ ). The three-fold contains the peripheral vortex layer, the core, and the annular zone. The peripheral layer is divided into several sections:

- A1: The part of shear layer, which is just shedded off from the edge; its starts off smooth but becomes wavy as it moves downstream.
- A2: The region where the shear layer breaks into little vortices that are evenly distributed throughout a smooth arc.
- A3: This is the region where as a consequence of interaction between the shedded tiny vortices lose their regular spacing. Because of the instability generated by the interaction, the position of these vortices may become chaotic.

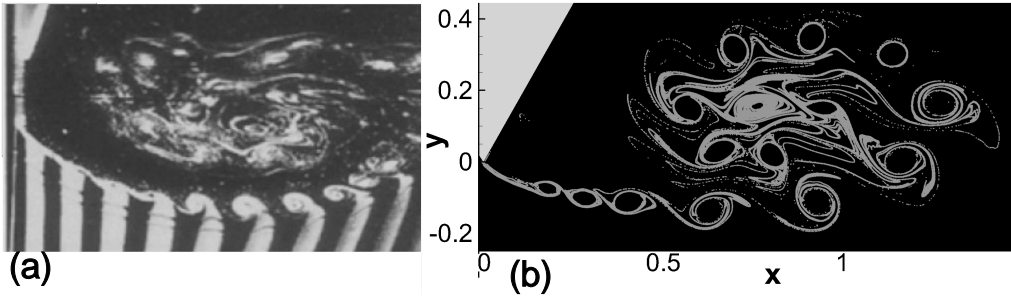


Figure 25: The third stage: Comparison of streaklines between (a) the experimental result of Lian and Huang (1989) ( $t = 2.885$ ) and (b) the present numerical simulation for  $Re_c = 6873$  at  $\tilde{t} = 20.57 \text{ sec}$  ( $t = 2.2$ ).

- A4: In this portion, the small vortices are scattered even more randomly.
- A5: It is located at the very end of the peripheral layer. The flow seems to be quite turbulent here.

The core can be divided into two parts: The Central core ' $C_1$ ' and the outer core ' $C_2$ '.

- $C_1$ : This core is formed owing mainly by the act of laminar diffusion. Viscous shear stress causes the concentrated vorticity of the initial spiral shear layer to diffuse. Since no apparent mass transfer is involved in the process, the shape of the spiral line remains undisturbed as shown in the the central part of the starting vortex in figure 25. However, the flow pattern surrounding this part appears very turbulent. This part is a rigid core.

- $C_2$ : It is the region around the undisturbed core and the streak lines appear very chaotic. However a close look at figure 23 would reveal that some instants earlier, in the same region ' $C_2$ ' the streak line used to be smooth, that implies there is no shear layer and no turbulent flow. Through a series of visualization, Lian and Huang (1989) had established that but some time before the event of figure 23(a), it was in fact turbulent, the turbulence appearance in the region  $C_2$  of figure 25 had germinated at that time. Thus the fluid in the outer core  $C_2$  has passed three stages; in the initial stage there were spiral shear layer (see the core in figure 21(b)), which then broke into turbulent flow (see the region just outside the core in figure 23(b)), and later, the turbulence has dissipated and the flow has again become laminar with distributed vorticity. This is the reason  $C_2$  is sometimes termed as a "relaminarized" region.

The region marked as  $B$  is the annular region which is turbulent in nature, a thin one and sometimes one can see this layer itself breaking into small vortices as in figure 23(a).

Thus, from the above discussion coupled with streakline visualizations of figure 25(a)-(b), it is clear that our simulation has very aptly captured all three stages of the evolution of the starting vortex leading to the three-fold structure which is exemplified by the comparison of our computed results with those of Lian and Huang (1989). To the best of our knowledge, for the flow past a mounted wedge, such structures have not been reported earlier. This further re-establishes the robustness of the scheme developed in Kumar and Kalita (2020), which despite being primarily developed for laminar flows, has remarkably resolved the early stages of turbulence as well.

#### 4.5.4. A short note on the long time flow evolution for $Re_c = 1560$

Our discussions so far in section 4.5 have been confined to flows for  $m \neq 0$  only. For  $m = 0$  and  $\beta = 1/3$ , description for the flow simulation for the initial stage could be found in the work of Xu (2016), albeit for an infinite wedge. Therefore, it would be interesting to see whether

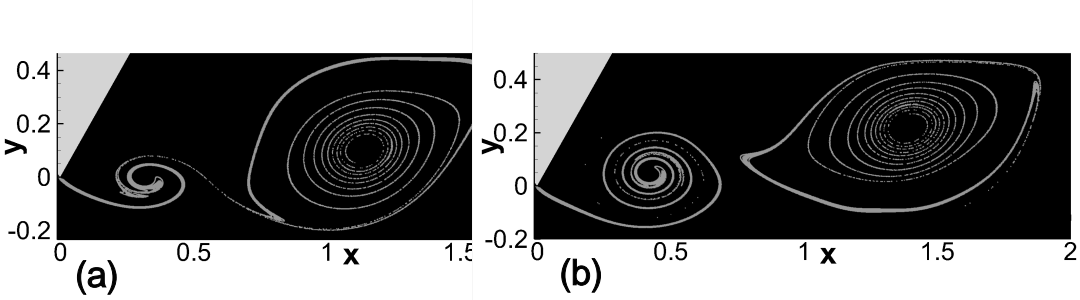


Figure 26: Streaklines for  $Re_c = 1560$  at instants (a)  $\tilde{t} = 100.79 \text{ sec}$  ( $t = 2.5$ ) and (b)  $\tilde{t} = 120.95 \text{ sec}$  ( $t = 3.0$ ).

the flow patterns observed in the second stage for  $m \neq 0$  are also existent for  $m = 0$  (uniform flow) as well or not. Here, the evidence of a full blown shear layer instability characterised by the double-branching structure was seen around a real physical time  $\tilde{t} = 100.79 \text{ sec}$  ( $t = 2.5$ ) for  $Re_c = 1560$  ( $m = 0$ ) as in figure 26(a). On the other hand, same was observed for  $Re_c = 6873$  at a much earlier time  $\tilde{t} = 19.91 \text{ sec}$  ( $t = 1.06$ ) as can be seen from the streaklines in figure 22(a). However for  $Re_c = 1560$ , the flow remained laminar for the whole duration of time for which simulation was performed as can be seen from figure 22(b) at time  $\tilde{t} = 120.95 \text{ sec}$  ( $t = 3.0$ ).

#### 4.6. Existence of Coherent Structures

Coherent structures are structures that remain in the flow for an extended period of time and are not merely a momentary phenomena (Hussain (1986)). Considering any two-dimensional turbulent flow; there are several structures that resemble vortices and remain in the flow for a short period of time. They will have a rotary motion and a circular appearance, and if they don't endure more than a few dynamical times, they will be ephemeral, non-coherent, and classified as Eddies. If, on the other hand, an 'Eddy' tends to stay for an extended period of time and does not appear to vanish, it is no longer an Eddy but a vortex, and it is no longer transient. These structures are coherent and can persist a viscous time scale or longer, depending on the conditions. Multi-scale vorticity fluctuations are a characteristic of turbulent flows. Several methods exist for identifying vortical coherent formations. Closed-loop streamlines and pathlines, minimum pressure areas, and absolute magnitude of vorticity are examples, however since they combine rotational motion and shear, these methods do not truly identify vortex cores. Nevertheless, Jeong and Hussain (1995) demonstrated that the second invariant of the rate of strain-tensor and the negative part of the second largest eigenvalue of the same tensor are reliable indicators of coherent structures in various flow situations. The second invariant in terms of streamfunction is given by the **Q criterion** (Benzi et al. (1987)).

A quick backdrop of this criterion could be given as follows. The eigenvalue analysis of the perturbed velocity field mentioned above, the eigenvalues are given by the formula  $\lambda = \pm\sqrt{Q}$ , where

$$Q = \left( \frac{\partial^2 \psi}{\partial x \partial y} \right)^2 - \frac{\partial^2 \psi}{\partial x^2} \frac{\partial^2 \psi}{\partial y^2}.$$

It follows that in the regions of the fluid where  $Q < 0$ , the distance between two particles embedded in the original velocity field will not diverge as a function of time. In figure 27(a), we plot the  $Q$  contours for the flow past a mounted wedge discussed in the previous

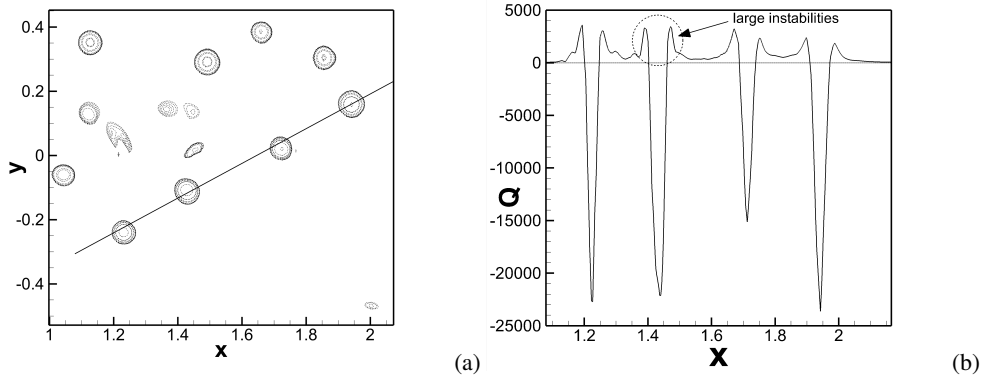


Figure 27: (a) Contour maps of  $Q$  at  $\tilde{t} = 24.31$  sec and (b) Distribution of  $Q$  along the line shown in (a) for  $Re_c = 6873$ .

section for  $Re_c = 6873$  at non-dimensional time  $\tilde{t} = 24.31$  sec ( $t = 2.6$ ) in a cross-section of the computational domain. Here, the dotted curves represent negative values of  $Q$  which corresponds to stable eigenvalues while solid curves represent positive values corresponding to unstable ones. As such the vortical shapes bounded by closed solid curves are coherent structures. One can see that these structures are always surrounded by dense negative contours indicating that large instabilities occur only at the edge of the vortices. This phenomenon can be understood more clearly by drawing a straight line through the centres of the coherent vortices (see figure 27(a)) away from the wedge in the region  $A_3$  of figure 24, and plotting the  $Q$  distribution along the  $x$ -coordinates of it as shown in figure 27(b). Here the segments of the graph below the zero-line represent the coherent structures. One can always see some oscillations on the edge of these structures just above the zero-line indicating the instabilities surrounding them. A similar procedure for the vortical structures resulting from the  $Q$ -contours for  $Re_c = 1560$  at  $\tilde{t} = 120.95$  sec ( $t = 3.0$ ) revealed no such instabilities. Thus our simulation has also resolved the existence of coherent structures in the flow field indicating the onset of turbulence for  $Re_c = 6873$ .

## 5. Conclusion

In this study, a recently developed second-order spatially and temporally accurate compact scheme on a non uniform Cartesian grid, developed by the authors, is used to simulate the complex fluid flow past a wedge mounted on a wall placed on a channel with wedge angle  $60^\circ$  for channel Reynolds number  $Re_c = 1560, 6621$  and  $6873$ . While the first  $Re_c$  corresponds to a uniform flow corresponding to a pre-chosen parameter  $m = 0$ , the latter two corresponds to accelerated flow corresponding to  $m = 0.45$  and  $0.88$  respectively. It is inspired by the famous 1980 laboratory experiment of Pullin and Perry (1980). To the best of our knowledge, this is probably the first time that for such flow situation, the boundary conditions used in the actual computation is such that it exactly mimics the physical situation used in the laboratory. Moreover, the authors are not aware of any numerical simulation for the flow past a wedge exactly of the current configuration for an value of  $m$  as high as  $0.88$ .

Our numerical simulation was able to replicate all the flow features of their laboratory experiment very accurately. A detailed account of the flow separation in the earliest part of the flow along with their time-line has also been provided. This includes tracking the trajectories of the vortex and rotation centers and comparing them with the laboratory experiment as well

as inviscid similarity theory. Our computed vortex center was found to be more closer to the scaling of the inviscid similarity theory than the experimental results. We also investigated the effect of the parameter  $m$  that determines the intensity of acceleration as well as the intriguing consequence of the non-dimensionalization typical of such flow configuration. Initially a weaker flow field was observed for the accelerated flow cases than the uniform one, marked by a reduction in the size of the starting vortices at non-dimensional time  $t < 1$  coupled with a weaker circulation. On the other hand, for  $t > 1$ , both the primary vortex center displacements and the size of the vortices are seen to catch each other. For  $m \neq 0$ , shear layer instability sets in very early in the flow, leading to more complicated vortex dynamics, indicating a transition towards turbulence.

The most significant achievement of the current study is, however, the simulation of the flow for a time range much beyond Pullin and Perry's experimental endeavour. The evolution of shear-layer instability leading to the onset of turbulence, characterised by the existence of coherent structures has been captured very aptly by our simulation. The accuracy of our simulation has been validated not only by the existence of coherent structures in the flow, but also by the remarkable closeness of our simulation to the high Reynolds number experimental results of Lian and Huang (1989) for the accelerated flow past a normal flat plate. All the three stages of vortex shedding, including the extremely complicated three-fold structure were resolved very efficiently.

#### REFERENCES

- DI Pullin and AE Perry. Some flow visualization experiments on the starting vortex. *Journal of Fluid Mechanics*, 97(2):239–255, 1980.
- Q-X Lian and Z Huang. Starting flow and structures of the starting vortex behind bluff bodies with sharp edges. *Experiments in Fluids*, 8(1-2):95–103, 1989.
- Ludwig Prandtl. Über flüssigkeitsbewegung bei sehr kleiner reibung. *Verhandl. III, Internat. Math.-Kong., Heidelberg, Teubner, Leipzig, 1904*, pages 484–491, 1904.
- Leo Anton. Formation of a vortex at the edge of a plate. Technical report, NATIONAL AERONAUTICS AND SPACE ADMINISTRATION WASHINGTON DC, 1956.
- E Wedemeyer. Ausbildung eines wirbelpaares an den kanten einer platte. *Ingenieur-Archiv*, 30(3):187–200, 1961.
- D Pierce. Photographic evidence of the formation and growth of vorticity behind plates accelerated from rest in still air. *Journal of Fluid Mechanics*, 11(3):460–464, 1961.
- Sadatoshi Taneda and Hiroyuki Honji. Unsteady flow past a flat plate normal to the direction of motion. *Journal of the Physical Society of Japan*, 30(1):262–272, 1971.
- SCR Dennis, Wang Qiang, M Coutanceau, and J-L Launay. Viscous flow normal to a flat plate at moderate reynolds numbers. *Journal of Fluid Mechanics*, 248:605–635, 1993.
- Heinrich Kaden. Aufwicklung einer unstillen unstilligkeitsfläche. *Ingenieur-Archiv*, 2(2):140–168, 1931.
- DI Pullin. The large-scale structure of unsteady self-similar rolled-up vortex sheets. *Journal of Fluid Mechanics*, 88(3):401–430, 1978.
- Jochen Kriegseis, Matthias Kinzel, and David E Rival. On the persistence of memory: do initial conditions impact vortex formation? *Journal of Fluid Mechanics*, 736:91–106, 2013.
- Matthew J Ringuette, Michelle Milano, and Morteza Gharib. Role of the tip vortex in the force generation of low-aspect-ratio normal flat plates. *Journal of Fluid Mechanics*, 581:453–468, 2007.
- P Koumoutsakos and D Shiels. Simulations of the viscous flow normal to an impulsively started and uniformly accelerated flat plate. *Journal of Fluid Mechanics*, 328:177–227, 1996.
- Henri Villat. *Leçons sur la théorie des tourbillons, par Henri Villat...* Gauthier-Villars et cie, 1930.
- Robert Krasny. Vortex sheet computations: roll-up, wakes, separation. *Lectures in Applied Mathematics*, 28(1):385–401, 1991.
- Peter A Davies, Julie M Dakin, and Roger A Falconer. Eddy formation behind a coastal headland. *Journal of Coastal Research*, pages 154–167, 1995.
- Ling Xu and Monika Nitsche. Start-up vortex flow past an accelerated flat plate. *Physics of Fluids*, 27(3):033602, 2015.



- Ling Xu. Numerical study of viscous starting flow past wedges. *Journal of Fluid Mechanics*, 801:150–165, 2016.
- M Kiya and M Matsumura. Incoherent turbulence structure in the near wake of a normal plate. *Journal of Fluid Mechanics*, 190:343–356, 1988.
- AE Perry and TR Steiner. Large-scale vortex structures in turbulent wakes behind bluff bodies. Part 1. Vortex formation processes. *Journal of Fluid Mechanics*, 174:233–270, 1987.
- Masaru Kiya and Mikio Arie. Discrete-vortex simulation of unsteady separated flow behind a nearly normal plate. *Bulletin of JSME*, 23(183):1451–1458, 1980.
- Reiyu Chein and JN Chung. Discrete-vortex simulation of flow over inclined and normal plates. *Computers & fluids*, 16(4):405–427, 1988.
- HR Tamaddon-Jahromi, P Townsend, and MF Webster. Unsteady viscous flow past a flat plate orthogonal to the flow. *Computers & fluids*, 23(2):433–446, 1994.
- Pankaj Kumar and Jiten C. Kalita. An efficient  $\psi$ - $v$  scheme for two-dimensional laminar flow past bluff bodies on compact nonuniform grids. *International Journal for Numerical Methods in Fluids*, 92(12):1723–1752, 2020.
- Murli M Gupta and Jiten C Kalita. A new paradigm for solving navier–stokes equations: streamfunction–velocity formulation. *Journal of Computational Physics*, 207(1):52–68, 2005.
- Jiten C Kalita and Murli M Gupta. A streamfunction–velocity approach for 2D transient incompressible viscous flows. *International journal for numerical methods in fluids*, 62(3):237–266, 2010.
- Shuvam Sen, Jiten C Kalita, and Murli M Gupta. A robust implicit compact scheme for two-dimensional unsteady flows with a biharmonic stream function formulation. *Computers & Fluids*, 84:141–163, 2013.
- Shuvam Sen and Jiten C Kalita. A 4OEC scheme for the biharmonic steady Navier-Stokes equations in non-rectangular domains. *Computer Physics Communications*, 196:113–133, 2015.
- John D Anderson Jr. *Computational fluid dynamics*. McGraw Hill, 1995.
- Richard H Pletcher, John C Tannehill, and Dale Anderson. *Computational fluid mechanics and heat transfer*. CRC press, 2012.
- Jiten C Kalita and Shuvam Sen. Unsteady separation leading to secondary and tertiary vortex dynamics: the sub- $\alpha$  and sub- $\beta$ -phenomena. *Journal of Fluid Mechanics*, 730:19–51, 2013.
- Wu-Ting Tsai and Dick K. P. Yue. Interaction between a free surface and a vortex sheet shed in the wake of a surface piercing plate. *Journal of fluid mechanics*, 257:691–721, 1993.
- A. K. M. Fazle Hussain. Coherent structures and turbulence. *Journal of fluid mechanics*, 173:303–356, 1986.
- Jinhee Jeong and A. K. M. Fazle Hussain. On the identification of a vortex. *Journal of fluid mechanics*, 285:69–94, 1995.
- R Benzi, S Patarnello, and P Santangelo. On the statistical properties of two-dimensional decaying turbulence. *EPL (Europhysics Letters)*, 3(7):811, 1987.